Evaluation of the Timing Characteristics of Various PET Detectors Using a Time Alignment Probe

Jason Hancock

Degree of Master of Science

Medical Physics Unit

McGill University

Montreal, Quebec, Canada

August, 2007

A thesis submitted to the Faculty of Graduate Studies in partial fulfillment of the requirements of the degree of Master of Science.

DEDICATION

I dedicate this thesis to my mother, Bonnie, for her support throughout all my post-secondary education. I would also like to thank my sister, Jodi, and my girlfriend, Taryn. Their support has made this achievement possible.

ACKNOWLEDGEMENTS

I would like to acknowledge my supervisor, Chris Thompson, for his help and support in my research and my writing and I wish him the best of luck in his retirement. As well, I have greatly benefited from conversations with my labmates, JoonYoung Suk and Katherine Woch, and my friend Darrel Hemsing.

ABSTRACT

Time alignment is performed on a conventional PET scanner in order to reduce the noise in the image from undesirable interactions, called randoms. In time of flight scanners this alignment is even more critical in order to place the position of an annihilation accurately. Traditionally, the alignment is an iterative process done by adjusting time offsets and recording the count rate until it is maximized. We have designed and built a positron detector that can be placed in the PET scanner. This enables each crystal in the scanner to be aligned to the same event (the positron detection), providing a constant reference to each crystal. This both increases the accuracy of the alignment and the speed in which it can be done.

ABRÉGÉ

L'alignement de temps est effectué sur un TEP conventionnelle pour réduire le bruit dans l'image causé par des interactions hasard. Dans les appareils utilisant le temps-de-vol, cet alignement est essentiel pour bien connaitre la position exacte de l'annihilation. Traditionnellement, l'alignement est un processus répétitif accompli en ajustant les décalés de temps et en enregistrant le taux de compte jusqu'il soit maximisé. Nous avons créé un détecteur de positron que nous pouvons placer l'intrieur du PET. Ceci nous permet d'aligner chaque cristal dans le scanner au même événement (la détection de positron), et de fournir une référence constante à chaque cristal. Ceci augmente la précision et la vitesse de l'alignement.

TABLE OF CONTENTS

LIST OF TABLES

LIST OF FIGURES

CHAPTER 1
Properties and Physics of Positron Emission Tomography

1.1 The Positron

The positron is the antimatter sibling of the electron. It shares all but one physical property with the electron. The electromagnetic charge of the positron is $1e$, while the charge of an electron is $-1e$. The mass of the positron is $0.511\frac{MeV}{c^2}$ and the intrinsic spin is $1/2$, mirroring the same values as the electron. The existence of the positron was postulated by Paul Dirac in 1928 as a result of his Dirac equation of relativistic quantum mechanics [1]. The particle was discovered in 1932 by the Swedish American Carl Anderson; for the discovery he won the Nobel Prize in 1936 [2]. Anderson studied the particle tracks left in lead from cosmic rays in a Wilson chamber. The Wilson chamber houses a magnetic field of 15,000 Gauss, and since the positron and electron are opposite charge, they will curve in opposite directions in a magnetic field. The length of the track ruled out the possibility it was made by a proton [3].

When, in material, a positron has a low enough energy (near or at zero), the positron can combine with an electron to form positronium. The real-matter equivalent of this atom is a hydrogen atom. Unlike a hydrogen atom, positronium is very unstable, with a maximum mean half-life of 140 nanoseconds (ns) [4]; The electron and positron spiral into each other and annihilate. The mass and minimal energy of the positron and electron is distributed to the products of the

annihilation. In most cases the products are two 511 keV photons that travel in opposite directions. A more rare case is three photons being produced. In accelerators hadrons may also be produced, but this is only in a laboratory setting [5].

1.2 Production of Positrons

There are three processes that produce a positron: Radioactive decay, pair production and triplet production.

Positron radioactive decay (commonly called beta plus decay) occurs in nuclides with an excess of protons in the nucleus [6]. This excess causes instability in the binding of the nuclear particles. To rectify this instability there are two decay modes available to the nucleus; one is electron capture the other is positron emission. Both these decay modes result in the atomic number of the nucleus (Z, the number of protons) decreasing by one, the atomic weight remaining the same (A, number of protons plus the number of neutrons) and the energy of the nucleus decreasing [7].

Electron capture can occur with any change in binding energy from the parent nucleus to the daughter nucleus, but for positron emission the difference must be at least 1.022 MeV. When beta plus decay occurs the parent nucleus decays to the daughter nucleus, a positron and a neutrino (${}^{A}_{Z}X \rightarrow {}_{Z-1}{}^{A}Y + \nu + \beta^{+}$); the energy of the neutrino and positron combined is the difference between the binding energies of the parent nucleus and daughter nucleus less 1.022 MeV [8], this is also the maximum energy of the positron. Some common positron emitters are shown in table 1–1. It is also important to note that even though the energy of the nucleus

is decreased through electron capture and positron emission, more energy may be given off in the form of gamma rays (for positron emission and electron capture) and characteristic x-rays and Auger electrons (both only in the case of electron capture).

Pair production and triplet production are similar photon interactions that occur in the Coulombic fields of subatomic particles. Pair production occurs in the field of the nucleus and triplet production occurs in the field of an orbital electron. During the interaction the photon vanishes and 2 particles are produced. In both interactions the particles are one electron and one positron; in triplet production the electron who's field the interaction took place in is ionized. Each process requires a minimum amount of energy of the incident photon, for pair production the threshold energy is 1.022 MeV and for triplet production it is 2.044 MeV [7].

1.3 Production of Radionuclides and Radiopharmaceuticals

Many radionuclides are found in nature. Although these were used in the early years of nuclear medicine, they are far from ideal for modern use [6]. Most naturally occurring radioactive substances have a very long half-life (millions to billions of years) or are heavy elements (such as uranium) and are not used in the metabolic processes in the body. A long half-life (the time it takes for half the unstable nuclei to decay) for an injected radionuclide would lead to a huge dose in the patient, possibly leading to radiation poisoning and many other potential problems. If the radionuclide is not used in metabolic processes it is not useful for any metabolic imaging and must then be attached to a pharmaceutical that is [9].

Radionuclide	Half-life	$E_{\beta,max}$ (MeV)	Production Reaction	Used to Image
^{11}C	20.3 min	0.961	$^{14}N(p,\alpha)^{11}C$ $^{10}B(d,n)^{11}C$	Lung cancer, Amino acids, Serotonin Synthesis, Brain tumours
^{13}N	10.0 min	1.19	$^{16}O(p,\alpha)^{13}N$ $^{12}C(d,n)^{13}N$	Myocardial blood flow, Brain tumor, Lung/ventilation
^{15}O	2.07 min	1.723	$^{14}N(d,n)^{15}O$ $^{15}N(p,n)^{15}O$	Brain blood flow
^{18}F	110 min	0.635	$^{18}O(p,n)^{18}F$ $^{20}Ne(d,\alpha)^{18}F$	Cancer, Neurological disorders, Myocardial diseases, Glucose metabolism

Table 1–1: Common Positron Emitters in Nuclear Medicine [9–18]

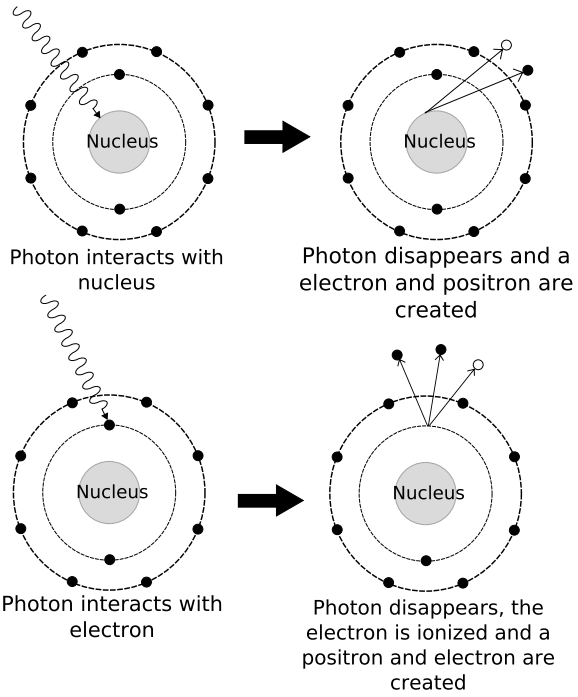

Figure 1–1: Diagram of Pair production (top) and triplet production (bottom)

Radionuclides commonly used in medicine are made artificially, with either nuclear reactors or particle accelerators. Nuclear reactors use enriched Uranium-235 (which has a half-life of 7×10^8 years) as a fuel source. When the Uranium nucleus undergoes fission two or three neutrons are also ejected. When thermal neutrons come in contact with ^{235}U it creates ^{236}U, which is very unstable. When ^{236}U undergoes fission, energy and neutrons are given off. Radioisotopes‘ are either from one of the fission fragments (of which there will be two) or from neutron activation (adding a neutron to the nucleus) by placing the element in the reactor. This method works well for creating neutron heavy radionuclides, used for beta minus (electron) emitters [9].

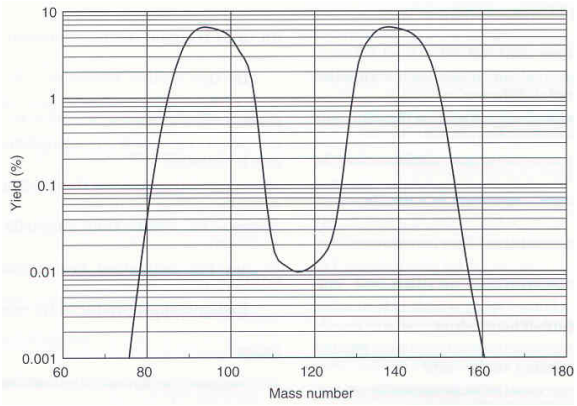

Figure 1–2: Mass number distribution of ^{236}U fission fragments. From Cherry et al. [9]

Positron emitting radioisotopes are created in a cyclotron. There are several designs of cyclotrons but each works on the same principle. A heavy charged particle (a proton or deuteron) is accelerated into a target element [16]. The acceleration is done by an alternating electric field, the path of the particle is controlled by a magnetic field. The bulk of the cyclotron is comprised by two large hollow semicircles called dees. The dees are connected to a alternating high-voltage. This alternating field causes an electric field in a space between the dees. It is in this space that the particles are accelerated. A magnetic field forces the particles to follow a circular path when inside the dees, containing the path inside the cyclotron (see figure 1–3. The centre of the cyclotron holds the ion source. For most PET isotopes a proton with two electrons ($^{-}$H) is accelerated through the cyclotron. Immediately before the collision with the target, the hydrogen nucleus is stripped of the electrons by passing the beam through a stripping foil (made

of carbon), then through the window. The interior of the cyclotron must be kept under a vacuum so the $^{-}$H does not interact with any other particles.

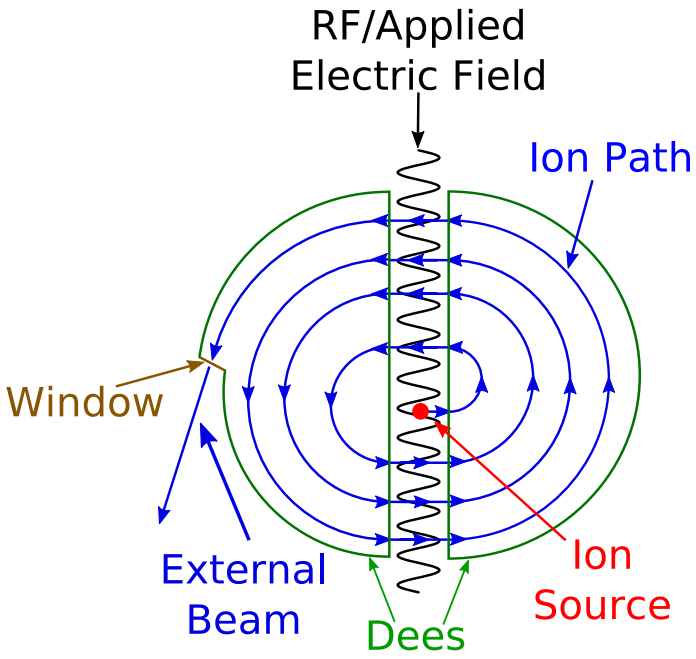

Figure 1–3: Top view of a cyclotron

There are several daughter radionuclides used in nuclear medicine as well, these are obtained from a radionuclide generator [19, 20]. The generator enables the separation and extraction of the daughter from the parent radionuclide which is produced in a cyclotron. The distribution is done in this method if the parent has a relatively long half-life and the daughter a short half-life. Since the parent decays much slower there is a longer lasting supply of the daughter radionuclide.

In general, the relationship for the activity of a radioactive substance is:

$$A = A_0 e^{-\lambda t} \tag{1.1}$$

where A is the current activity, A_0 is the initial activity, λ is the decay constant of the radionuclide and t is the time that has passed. When the half-life of the parent is much longer then the half-life of its daughter (such as the situation in a generator) an equilibrium is reached called transient equilibrium [21].

$$A_d = \frac{\lambda_d}{\lambda_d - \lambda_p} A_{p,0}(e^{-\lambda_p t} - e^{-\lambda_d t}) \tag{1.2}$$

where p represents the parent and d represents the daughter.

In order to image the metabolic processes in the body the radionuclide must trace a metabolic process. This is done by attaching (or labeling) the radioactive atoms to metabolic compounds to form a radiopharmaceutical [6]. The radioactive atom can either replace a stable version of itself (as is often done with ^{11}C, ^{13}N and ^{15}O) or can replace a similar atom or group in a compound (as is done with ^{18}F) [9]. Once the radiopharmaceutical is prepared it can be injected into the patient and the level of concentration can be detected.

1.4 Basics of PET

The primary concept of positron emission tomography (PET) imaging is to determine the distribution of a positron emitting radioisotope throughout the object being imaged. In PET this is done by placing the object into a ring of detectors and measuring the number of annihilation photons that are detected [6]. Since the photons from an electron-positron annihilation travel anti-parallel to each other, one can determine the line where the annihilation occurred by knowing which detectors the photons interacted with. Note that this method actually images the distribution of the annihilation events. Since the positron is emitted

from the nucleus with a non-zero amount of energy, the annihilation does not occur where the nucleus is. This is a source of blurring in PET imaging [6].

Energy information is used to determine if an event in a detector should be accepted or rejected [6]. Compton scattering (see figure 1–9) causes a photon to lose energy and change direction, in this case it will cause the energy of the photon to be less then 511 keV. If the photon has been scattered the position information will be incorrect and the larger the scattering angle is; the farther from 511 keV the photon energy will be (see equation 1.3). Also, it is probable for two photons to strike the same detector at the same time, if this happens, the energy they deposit will be summed and may result in an energy above 511 keV. The scattered photons and dual photons are events that are not desired to form the final image. Since the detectors can not determine the energy of a photon with absolute precision, a window of acceptable energy values is used: this window is roughly centered at 511 keV. A common energy window is from 350 keV to 650 keV; all events in that energy range will be accepted and pass to the timing discrimination [22].

The two photons from an annihilation will travel at the speed of light and will hit a detector at nearly the same time. If the annihilation happens at the midpoint between the detectors the time should be identical and any offset from this will result in a small time difference. In order to differentiate two separate annihilations, only events within an acceptable timing window will be registered [6]. As with the energy information, the timing information is inexact, necessitating the need for an acceptable range of timing differences. The width of the timing

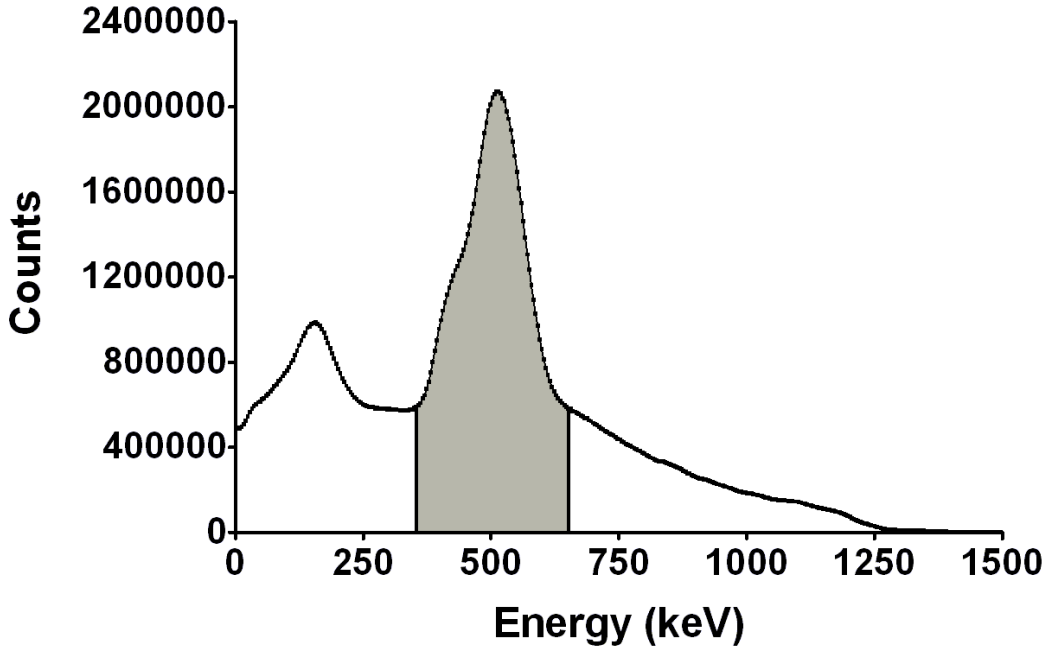

Figure 1–4: Sample of an Energy Spectrum and its Discrimination Window

window is dependent on the type of detector and size of detector ring, but common values are 6 ns or 12 ns [22]. The timing window is centered at a timing difference of zero. If two events occur within this timing window and within the energy window they are added to the events that will make up the image.

1.5 Event Types

There are three types of events that can be registered in PET imaging: True events, scattered events and random events. A true event is the result of two photons from the same annihilation that have not been scattered and each photon is falls within the energy and time window. These events compose the useful, good image.

A scattered event contributes noise to the final image and reduces the contrast. When a photon is Compton scattered its energy will change (see equation 1.3), but possibly not enough to place it outside of the energy window. If the photon's energy still places it within the energy window and both photons are detected within the timing window, the event will be added to the image. Since the one photon had been scattered and changed direction the position of the annihilation will be wrong, this degrades the image.

$$h\nu_{\text{lost}} = h\nu_{\text{initial}}\Big(1 - \frac{1}{1 + \epsilon(1 - \cos\theta)}\Big) \tag{1.3}$$

where $h\nu$ is the photon energy, ϵ is the ratio of the photon energy to the rest mass energy of an electron (511 keV) and θ is the angle of deflection of the photon [23].

The remaining event type, a random event, also serves to degrade the image [6]. When two annihilations happen at near the same time there will be four photons released. One photon from each of the two different annihilations can be detected in coincidence with each other, this will also place the annihilation at the incorrect position. The rate of random events ($\dot{R}$) is proportional to the size of the timing coincidence window (τ)

$$\dot{R} = 2\tau\,\dot{C}_i\dot{C}_j \tag{1.4}$$

Where $\dot{C}_i$ and $\dot{C}_j$ is the singles rate of detector i and j, respectively [22]. Since the rate of randoms is dependent on the singles rate of each detector, the randoms rate increases quadratically with the amount of activity being imaged, while scatter and randoms increase linearly with activity (see figure 1–6).

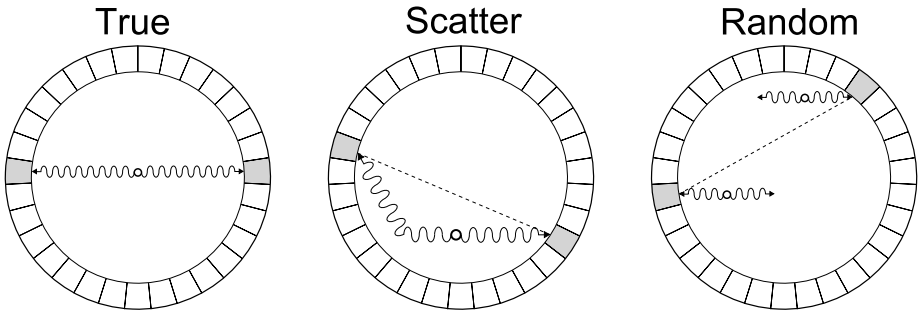

Figure 1–5: The three types of PET events

The ratio of the three types of events depends on the type of scan being performed (brain scan, whole body, 2D, 3D...) and on the amount of activity that has been injected into the patient. For a typical brain scan the ratio of randoms to trues is from 0.1 to 0.2, but in whole body scan this number is substantially increased and is more then 1. The scatter to trues ratio is independent of activity but has a strong dependence on the use of interdetector septa (thin sheets of metal to absorb scattered radiation) [22].

The noise equivalent count rate (NECR) is a parameter used to evaluate PET performance [24, 25]. The value is a relation between the trues, randoms and scatters and the objective is to maximize this value. The NEC (noise equivalent counts) is as follows:

$$NEC = \frac{T^2}{T + S + 2fR} \ , \tag{1.5}$$

Where T, S and R are the true counts, scattered counts and random counts and f is the fractional field of view [26].

PET imaging takes longer to perform then CT and MRI. In order to reduce the noise and improve the statistics many coincidences must be used; to increase

the coincidences and decrease the scan time a high amount of activity may be injected. Unfortunately, due to the quadratic nature of the randoms counts (figure 1–6), this may not result in less noise. The NERC has a maximum of activity concentration (which depends on the scanner) that results in the optimal image [24]. Since random counts are also dependent on the width of the timing coincidence window (see equation 1.4) the NECR can be optimized at a higher activity (and shorter scan time) if the timing window is made narrower [22].

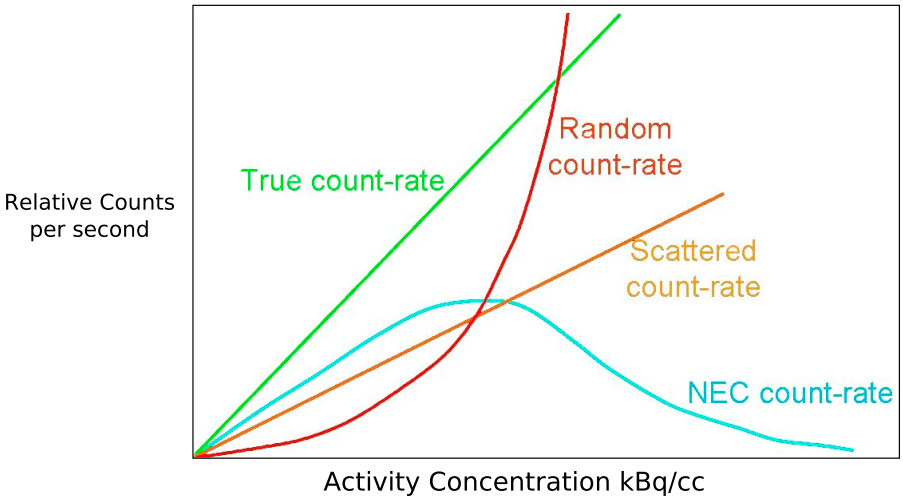

Figure 1–6: Response of events to activity

The two main contributions to the width of the timing window are the time resolution and the time alignment. The time resolution is a property of the system based on the scintillators used, the photomultiplier tubes and the electronics. The more accurately the time of an event is recorded by the system the better the time resolution. Normal values of time resolution range from ∼500 ps to ∼5 ns. These values are taken as the full width at half maximum (FWHM) of a timing spectrum (see figure 1–7). The better the time resolution is the more potential the

system has to have a narrow timing window and employ more advanced imaging techniques such as time of flight PET.

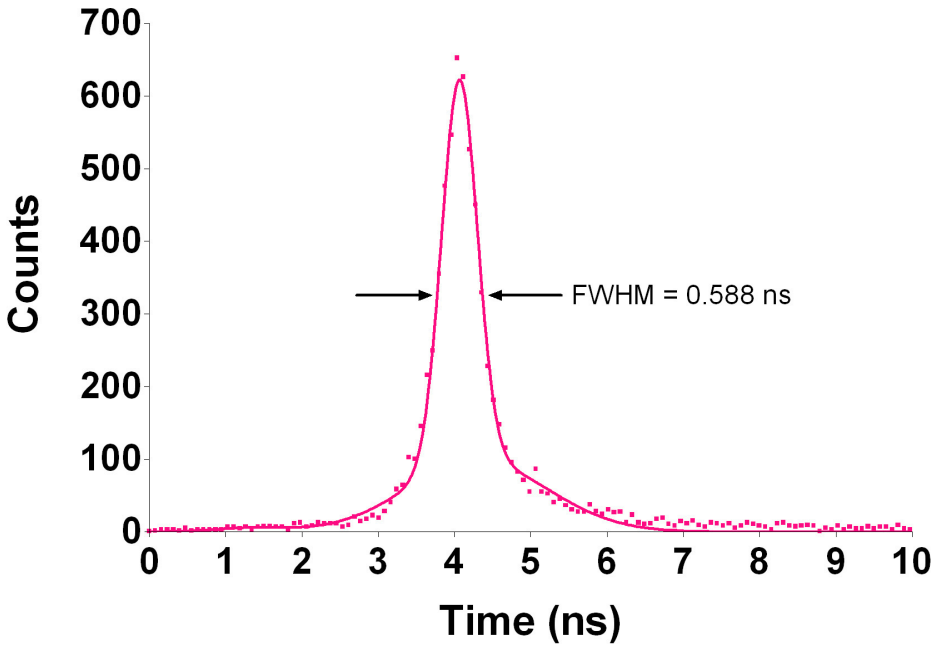

Figure 1–7: Sample of a timing spectrum and the FWHM resolution

Variations in cable lengths, individual PMT properties, individual crystal properties and electronic differences result in two temporally aligned events being recorded at different times. The alignment obtains the time offsets that should be set to each detector in order to have the events recorded with the same time stamp. There are several methods that are used to obtain the offsets (discussed in chapter 2), but the most common method is done iteratively and is very time inefficient resulting in the alignment being done rarely. The adjustments needed

can change over time, so performing the alignment occasionally is beneficial to the operation of the PET scanner.

1.6 Detectors and Scintillators

The most important component of a PET scanner is the detector. In general, a detector consists of scintillators to convert the high energy photons to visible (or near-visible) light and photomultiplier tubes (PMTs) to convert the visible light into an electrical signal. In order to maximize to efficiency of a scanner the physical properties of the scintillator must be optimized. To maximize the amount of energy extracted from the photon, the effective atomic number (Z) and the mass density should be as high as possible. The energy resolution of the scintillator is dependent on the light output of the scintillator so the light output of the scintillator should be as high as possible. Other important factors are the decay time and the index of refraction. Of course, to transmit the light, the scintillator must be transparent.

At 511 keV the annihilation photons will interact with the scintillator through Compton scattering, Rayleigh scattering and photoelectric absorption [7]. When a photon undergoes the photoelectric effect, all of its energy is transfered to an electron and the photon disappears. If the photoelectric absorption is the first interaction an unscattered photon undergoes in the scintillator, the entire photon energy is deposited at the same time, resulting in the energy being measured as 511 keV (or close to it with statistical variation and electron binding energies). Since the energy window is centered at 511 keV this is the optimal value, thus making the photoelectric effect the desired interaction in a scintillator. If all

photons underwent photoelectric absorption on the first interaction all events would deposit their energy in the 511 keV peak and be within the energy window. The photoelectric cross section (probability of photoelectric interaction) is strongly dependent on the atomic number (or effective atomic number) of the scintillator, varying from Z^4 for low Z materials to $Z^{4.8}$ for high Z materials [8].

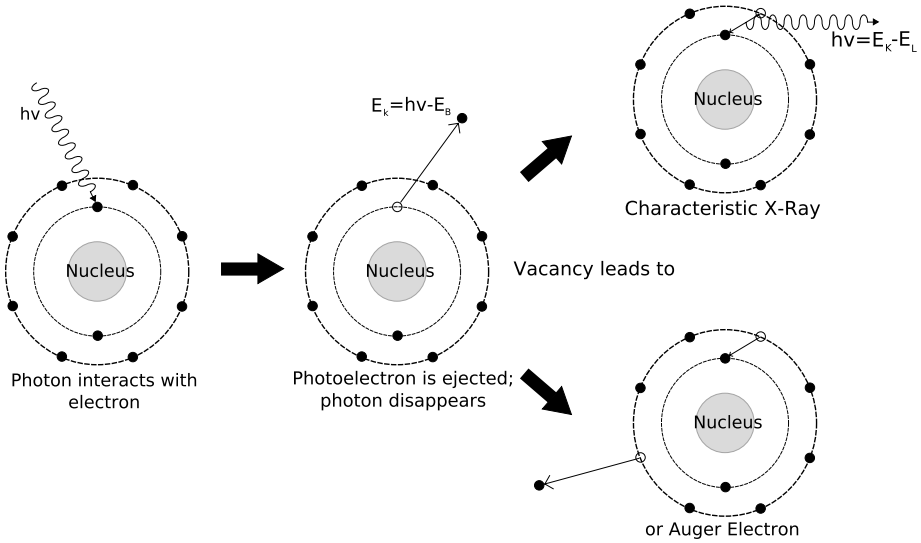

Figure 1–8: The Photoelectric Process

Although the energy spectrum has the best results when the photon undergoes a single photoelectric event, this will not happen enough so that Z is the only important parameter. Stopping power describes the amount of energy lost per length in a material. Collisional stopping power is the amount of photon energy lost to the material that results in energy being deposited in the scintillator. The collisional stopping power is dependent on the density of the material (ρ), and it is desirable to have as large as possible [7].

When a photon undergoes Compton scattering, energy is transfered to a free electron (an electron with a much lower energy then the photon) and the photon loses energy and changes direction [7]. If the photon undergoes a Compton scatter in the scintillator and then leaves the scintillator, the energy deposit will not be complete. Since Compton interactions are very likely, there are many detected photons that are not scattered in the body but should be counted, so the energy discrimination window is left wide enough to include the internal detector scatters with larger energy deposits (figure 1–10). The inclusion of these interactions also implies that some photons from externally scattered events (with incorrect positional information) will also be included. In order to form a reasonable image in a reasonable time the energy window must be wide.

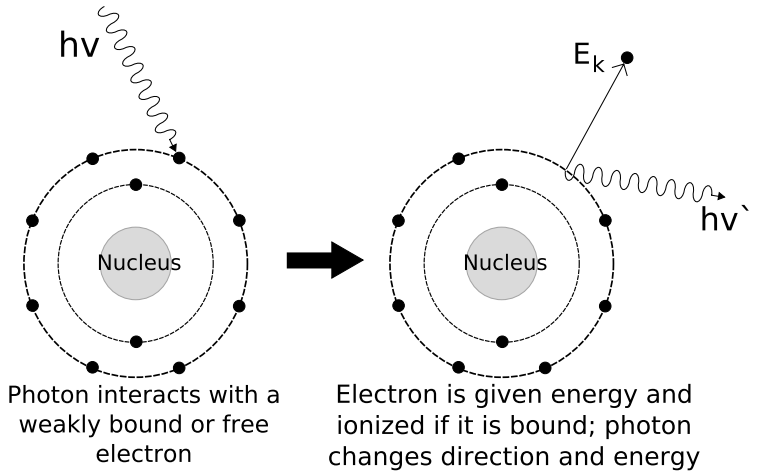

Figure 1–9: Compton Scattering

The third type of interaction that can occur in the scintillator has minimal effects on the image quality. When the photon interacts with a bound atomic electron and scatters this is called Rayleigh scattering. Very little energy is

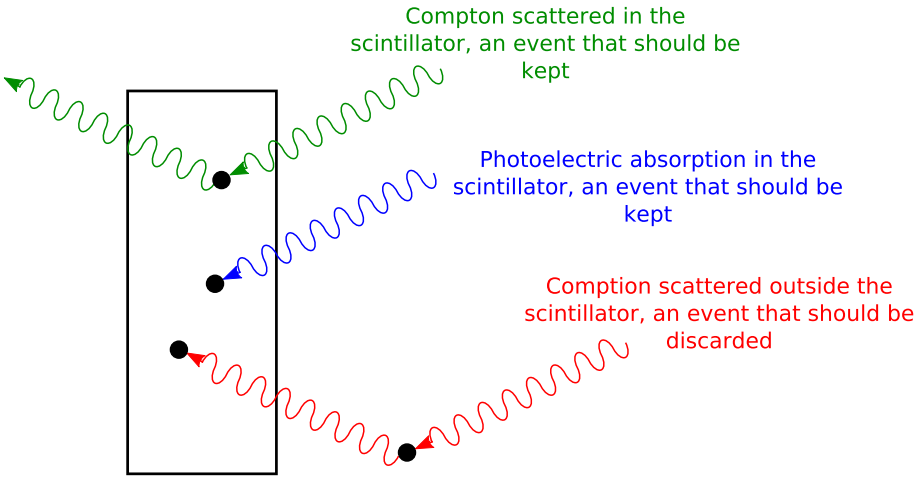

Figure 1–10: Good and bad scattering events

transferred to the electron and it does not ionize. The photon loses very little energy and has a very small change in direction [7]. The momentum from the direction change is absorbed by the atom. Since there is little energy lost and little directional change, this interaction is not a significant event in the scintillator.

Table 1–2 shows various properties for several scintillators that are used in PET and nuclear medicine. The density of the material and the effective atomic number each influence the detection efficiency of the scintillator. The highest density materials are BGO and LSO, which also have the highest effective atomic number. For these reasons LSO and BGO have become, by far, the most common scintillators in commercial PET systems. The decay time effects the potential time resolution of a system, where a short decay time is most desirable, BaF_2 is the crystal with the fastest decay time, LSO is the fastest common commercial scintillator. Energy resolution has a very strong dependence on the light output of a crystal, which gives $LaBr_3$ a great energy resolution. LSO is the common

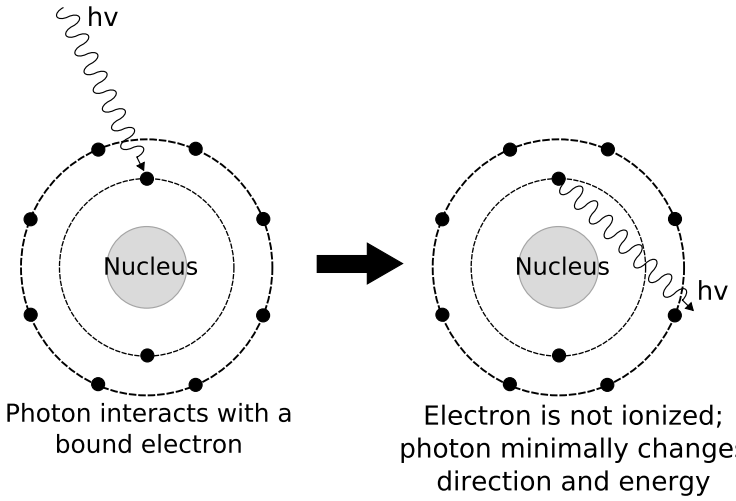

Figure 1–11: Rayleigh Scattering

commercial scintillator with the best light output, and it is one of the best in the table, but its energy resolution is degraded by its intrinsic radioactivity from Lu. The wavelength of maximum emission is most desirable around 420 nm since this is the wavelength that is most permissible through glass, a common and inexpensive window in photomultiplier tubes. LSO exactly matches this wavelength. Also useful because of the window, is an index of refraction of around 1.6, since this also matches glass, and will result in the least light loss when the light passes from the scintillator to the PMT. Finally, if a crystal is hygroscopic, it implies that it will easily absorb water, which, over time, will degrade the transparency of the crystal and decrease its efficiency. If a crystal is hygroscopic, it must be air-sealed from the environment [27].

Once the scintillator has converted the high energy photons to many low energy photons they must be converted into an electrical signal or pulse [28]. This is done by a photomultiplier tube (PMT) via a light guide (or light pipe) [6]. The

simplest method to move the light from the scintillator to the PMT is by attaching them with scintillator glue. The scintillator is mounted directly onto the face of the PMT. If the size and/or shape of the faces do not match, or in other housing geometries, this may not be possible. The output of the PMT is dependent on the magnetic field it is in, so it is desirable (if not necessary) to have the PMT as far as possible from a magnetic field [29]. If measurements are done in a strong magnetic field a light guide is used to have the scintillator in the magnetic field, but the PMT removed from it. A light pipe must have as much total internal reflection as possible to maximize the amount of light reaching the PMT. To do this the surfaces should be polished and coated with a reflective surface. A common solid light guide is Lucite. Fiber optic cables can also be used if arranged correctly [27, 30].

Scintillator	BGO	LSO	NaI	BaF_2	GSO	$LaBr_3$	LYSO
Chemical Composition	$Bi_4Ge_3O_{12}$	Lu_2SiO_5:Ce	NaI(Tl)	BaF_2	Gd_2SiO_5:Ce	$LaBr_3$(Ce)	$Lu_{1.8}Y_{0.2}SiO_5$:Ce
Density $\left(\frac{g}{cm^3}\right)$	7.1	7.4	3.7	4.9	6.7	5.3	7.1
Decay Time (ns)	300	40	250	630 (slow) 0.6-0.8 (fast)	60	16	41
Light Output $\left(\frac{Photons}{keV}\right)$	9	26	38	10 (slow) 1.8 (fast)	8	63	32
Wavelength of Max Emission (nm)	480	420	415	310 (slow) 220 (fast)	440	380	420
Refractive Index	2.15	1.82	1.85	1.50 (slow) 1.54 (fast)	1.85	1.9	1.81
Hygroscopic	No	No	Yes	Slightly	No	Yes	No
Z_{eff}	75	65	51	53	59	47	48-66

Table 1–2: Scintillators Used in Nuclear Medicine and their Properties. Note that the fraction of Yttrium to Lutetium in LYSO was in the crystals used in these studies, the ratios may be different for different crystal manufacturers, and, as a consequence, the effective atomic number is given as a range (Lu from 15% to 100%) [22,31–37].

The PMT is the primary device used to convert a scintillator pulse to an electrical pulse [28,38,39]. The conversion from photons to electrons is done with a photocathode commonly made of a multialkali material (Na_2KSb) or a bialkali material (K_2CsSb). The choice of photocathode is strongly dependent on the peak of the emission spectrum from the scintillator. In order for a photon to be converted to an electron, the energy in the photon must first be transferred to an electron, then electron must migrate to the surface of the photocathode then escape the surface. Each of these three step presents probable energy loss. Initially, the energy that the photon gives the electron must be enough to ionize it; then the electron must maintain enough energy through electron-electron collisions in the photocathode; and finally it must have enough energy remaining to overcome the work function: the energy barrier for an electron to escape the surface. The work function can range from 1.5-4 eV, ideally it will be from 1.5-2 eV. The energy the photons transfers to the electron is dependent on the scintillator but is on the order of 5 eV [27].

One high energy photon will lead to many low energy photons, once the electrons produced by those photons have escaped the photocathode they need to be amplified to produce a signal. This is achieved through a series of dynodes (see figure 1–12). Each dynode has the property of emitting several electrons when it is struck. The dynodes are held at a high voltage ($\sim$150 V between each) in order to accelerate the electron into it's surface. The process of this is similar to that of converting a photon to an electron, but now it is converting an electron to more electrons [38]. The multiplication by each dynode is dependent on the material it is

made of and the applied voltage, but a reasonable value is 5 electrons for each that strikes the surface. The number of dynodes in the series depends on the desired properties of the PMT but is usually around 10; this results in a multiplication of about 10^7 for each electron that escapes the photocathode [27].

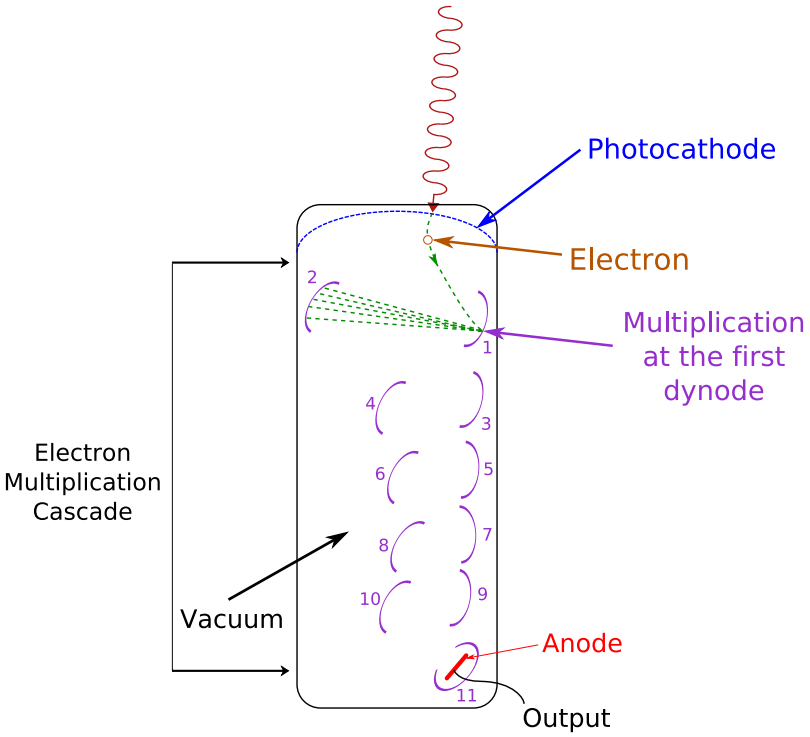

Figure 1–12: Basic design of a Photomultiplier Tube [27]

The orientation and placement of the PMTs and scintillators in a PET scanner is done in a design called a block detector. This consists of a large block of scintillator crystal (2 cm x 2 cm to 3 cm x 3 cm and 2 or 3 cm deep [22]) which may be cut partially through the depth to create many individual elements on a single crystal face. The small crystal elements serve to increase the spatial resolution of the detector. In the cut out regions a reflective material is inserted so

that light is not lost [6]. A single block detector will consist of an array of crystal elements about from 4 x 4 to 16x16, or 16 to 256 individual elements (see figure 1–13 and 1–14). If you were to couple each crystal element to a PMT this would result in 16 to 256 PMTs for each of the approximately 500 block detectors in a PET scanner. This is an enormous number of photomultiplier tubes and would be very expensive and also require very small PMTs. As a compromise each array has four large PMT's attached to it and Anger logic is used to place the event in the crystal array. Anger logic is a simple ratio of the signals from the individual PMTs over the sum of the signal from all the PMTs in the detector (see equations 1.6 and 1.7) [40].

$$X = \frac{(B + C) - (A + D)}{A + B + C + D} \tag{1.6}$$

and

$$Y = \frac{(C + D) - (A + B)}{A + B + C + D} \tag{1.7}$$

where A+B+C+D is the energy that is sent to the energy discriminator.

1.7 Specialty Detectors

It is important to note that a PET image is used to acquire metabolic information, it may or may not contain anatomical information. If anatomic information is required (such as in preparation for radiation therapy) then a MR or CT image is required. A widely used method to obtain both metabolic and anatomical images is a combined PET/CT scanner. Both the PET scanner and CT scanner are built into one scanner, this helps with image registration and minimizing movement and misalignment between the scans. An obvious

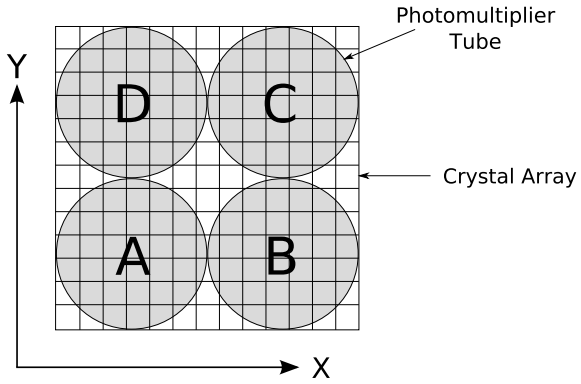

Figure 1–13: Top view of the block detector design, with the four PMTs (A,B,C & D)

analogue to this is a combined PET/MRI scanner. Since MR has better soft tissue contrast and gives no dose to the patient (unlike the large dose from CT) this is a desired technology. A CT scan is much faster than an MR scan, but since a PET scan takes a long time, this is not an important advantage for CT over MR in a multimodality scanner.

On the surface the integration of PET technology and MR technology seems like it should be similar to the integration of CT and PET, but it is not. MR scans are performed in a very large magnetic field; this magnetic field vastly degrades the performance of photomultiplier tubes. There have been two solutions to this problem; one is to optically couple the scintillators to the PMTs with fiber optic cables. The cables would be long enough so the PMTs are not in the magnetic field. This is not practical though since a full multi-slice scanner would require a very large amount of cables and the light loss in the transfer degrades the image. The other solution is to use a semiconductor to convert the light to an electrical signal [41].

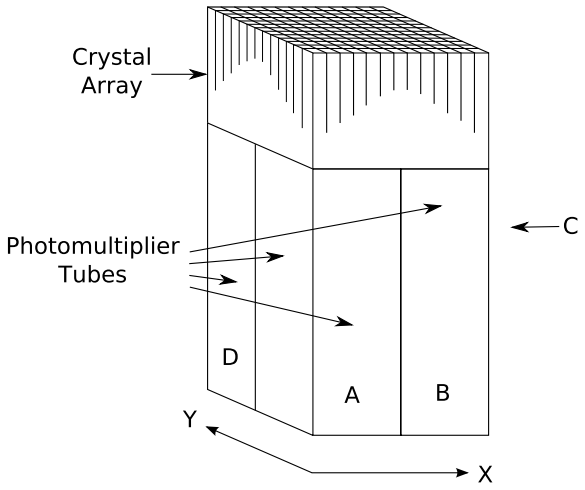

Figure 1–14: 3D drawing of a block detector

Avalanche photodiodes (APDs) are the common replacement for a PMT in a magnetic field. The APD uses doped semiconductors to convert the light into electrical pulses (see [27]). Since the operation of the APD is not effected by an external magnetic field it is useful for a PET/MR scanner. When light goes into the P-N junction in the diode it may create an electron-hole pair. The electrons and holes will migrate against and with the applied electric field, respectively. If the applied field is large enough the electron will create more electron hole pairs, effectively amplifying the pulse generated. These pulses generate the signal. Since the distance traveled by the electron hole pairs is very short and the electric field is very strong, the magnetic field has nearly no effect on the operation. The energy of the photon needed to generate the first electron-hole pair is dependent on the semiconductor, but for Silicon it is 1.12 eV [42].

Not only do the MR properties effect the PET equipment, the opposite is also true. There are three magnetic fields used in a MR scanner, one very large

one and two smaller fields. The homogeneity of the large field is very important and the PET components that are used need to retain this homogeneity as much as possible. As well, the RF pulses used in the MR operation are detected by the amplifiers for the PET electronics, this causes the need for shielding of those.

Common scintillators in both PET and SPECT (single photon emission computed tomography) were tested for their magnetic susceptibility in differing magnetic fields. Table 1–3 shows the susceptibility for several scintillators in 0.5 T magnetic flux density; the NaI crystal is hygroscopic, so it is sealed with a metal, tested were aluminum and copper casings. The images from common MR pulse sequences were also examined for artifacts. Only GSO and LGSO showed significant artifacts in the MR image. The ideal magnetic susceptibility is as close as possible to human tissue (-7×10^6 to -11×10^6). The scintillator used most often in PET/MRI is LSO for it's superior light output, short decay time and reasonable susceptibility [43].

	NaI-Al	NaI-Cu	CsI	BGO	LSO	LGSO	GSO
Magnetic Susceptibility ($\times 10^6$)	3.8	-13.2	-19.6	-19.0	-21.7	790	9530

Table 1–3: Susceptibility of Various Scintillators [43]

1.8 Image Reconstruction

The process of forming an image from a PET data set requires many steps and other scans to be done. First a normalization correction is required. This is a simple scan that allows the user to account for non-uniformity in the thousands of detectors. Among detectors there are small differences that result in different

light output and time response during a scintillation and through the electronics. This variation can cause a higher or lower count rate when exposed to the same activity and is the reason for normalization. To get a normalization factor for each line-of-response (LOR) a positron emitting rod source or a uniform positron emitting cylinder, is put in the field of view (FOV) and that scan taken. The ratio of the average count to the actual count is the correction factor for that LOR. [22]

Attenuation correction is the most important correction to PET data. This corrects for the attenuation of the photons by the object being imaged. Most simply this data is acquired by running a scan with nothing in the FOV and activity provided by a positron emitting source that orbits just inside the detector radius (but out of the FOV), called a blank scan. Once completed the same scan is done but now with the object or patient to be imaged in the FOV, called a transmission scan. The attenuation correction factor (ACF) is ratio of the blank scan count rate to the attenuation scan count rate across each LOR. [22]

While this method results in the most accurate ACFs and is the simplest, it is also the most time consuming and requires the patient to be in the scanner for a very long time, for this reason it is very seldom used clinically, but is required for certain images such as dynamic scans or scans using an radioisotope with a very short half life. Other methods are post-injection scans or simultaneous emission/transmission scan. When these methods are used one blank scan is done in the morning and used throughout the day. The transmission scan for each patient is obtained either before or after the PET scan. Since the transmission data must be accurate the activity of the transmission source is much higher then

the activity of the injected radiopharmaceutical. The higher activity results in less noise when the emission data is subtracted from the emission+transmission data [44]. A common transmission source for this method is germanium 68 [22].

Another method to obtain the transmission data is to do an emission/ transmission scan using a orbiting single photon emitting source. In order for this to be useful the photon that is emitted must be accepted by the energy discriminator, and therefore reasonably close to 511 keV. The difference in the energy from the single photon in the transmission source to the 511 keV photons from the radiopharmaceutical results in less data needed from the emission/transmission scan. This decrease is because of a more accurate subtraction of the emission data caused by fewer counts from the 511 keV photons in the single photon energy channel. Often used as a source is Cesium 137 which has a single photon energy of 662 keV [22]. Since 662 keV photons will be attenuated differently then 511 keV photons the attenuation values must be scaled from 662 keV to 511 keV, and although this scaling is not linear, it is well known and simple. In small animal imaging Cobalt 57 is used as the transmission source, since the photon energy of Cobalt 57 is much lower then Cesium 137 (122 keV to 662 keV) there is much better soft tissue contrast [45]. Once the attenuation image is obtained each part of the image is assigned an attenuation coefficient for 511 keV based on what tissue it is. In order to assign a tissue to a pixel a range of values is given to discriminate it from others (eg. bone, lung, soft tissue); this method is segmented attenuation [46].

The other corrections that need to be performed before image reconstruction are dead-time correction, random correction and scatter correction. Dead-time

is the amount of time a counting system takes to detect and record an event. When one event is detected the detector that is in use is unable to detect and record another; therefore the larger the detectors are in a scanner the more dead time it has [6]. At clinical levels of activity this is not a large problem, but can become one at higher activities. There are several methods to correct for scatter, and these differ for 2D and 3D scans. In 2D scans a portion of the data is fit to a mathematical function and just subtracted, the data removed is the scattered data. In 3D scans this can apply as well, but it much more complex. More common methods are to take Monte Carlo data and use that to subtract the scattered information or to have the image reconstruction algorithm compensate for scatter [22]. Random correction, which is applied before scatter correction, is discussed in chapter 2.

The information from a 2D data set is stored in a histogram with an x-axis of r (distance from the origin) and a y-axis of ϕ. The histogram is known as a sinogram. Each column of the sinogram (constant ϕ) represents a projection at a single angle [6]. For the complete set of data from a 3D scan a set of sinograms are needed. In this case each sinogram has the same x and y axes, but represents the projection set a polar angle θ.

A problem arises when trying to reconstruct 3D data. Reconstruction methods, primarily because of Fourier transforms, rely on a complete set of data in order to be done properly. The data sets from 2D scans accomplish this because of the complete sampling of the radial space, but in 3D scans, the axial dimension is not and can not be completely sampled. There are 2 methods used to rebin the 3D

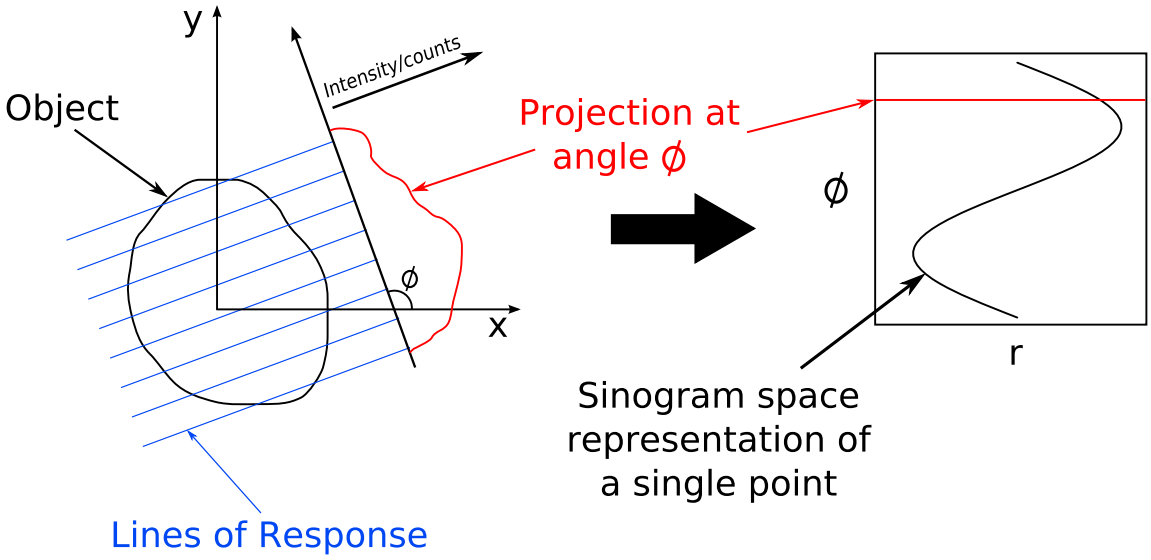

Figure 1–15: PET projections and data storage in sinograms

data for reconstruction; these are Fourier rebinning (FORE) and three dimensional rebinning (3DRP). These methods are slow and requite the complete 3D data set (which is large) [22,47]. The other option is to rebin the 3D data set into 2D data sets. This method essentially assigns the cross-ring data into 2D data slices. This method allows for 2D reconstruction algorithm use and also results in much smaller data sets. The method commonly used clinically is FORE [22].

For reconstructing 2D data sets there are two primary methods. One algorithm used is filtered back projection (FBP). This algorithm transforms the projections from real space to frequency space through a Fourier transform, applies a filter, then back projects the projections into image space [6]. Scanner geometry, sensitivity and the activity used are a few of the considerations taken into account when choosing the correct filter. The other method for reconstruction is maximum likelihood expectation maximization (MLEM) or ordered subset expectation

maximization (OSEM), a modification of MLEM. These methods are computer intensive and iterative algorithms designed to maximize an approximation to the image, once the approximation to the real activity distribution is found, that is the image used. Limits are set for this reconstruction of what constitutes an acceptable approximation of the real data set [22, 48].

CHAPTER 2
Time Resolution, Timing Alignment and Time of Flight PET

2.1 Time Alignment

In its simplest terms timing alignment is the ability of two detectors to report two temporally aligned detections as happening at the same time. If each detector has a photon interact with it at the same time, then, through the path of the PMT and the electronics, the two events should record an identical time stamp for the time of their interactions. Small deviations in the time stamp are acceptable as a consequence of imprecise timing information from the scintillator, PMTs and electronics, but systematic differences are not acceptable. The small stochastic deviations are a result of the non-zero time resolution and it is dependent on the scintillator used and the characteristics of the PMTs as well as the electronics used to process the signals. The better the time resolution is the more accurately the time of the event is known. The systematic differences can be the result of cable length differences, individual PMT gains and electron propagation, scintillator light output [49] and quality of electronics.

The amount of noise in an image is reduced when the detectors are better aligned. This reduction is due to a more narrow timing acceptance window. The narrower window has the purpose of reducing the number of random coincidences while minimally effecting the number of true coincidences (see figure 1–5 for a

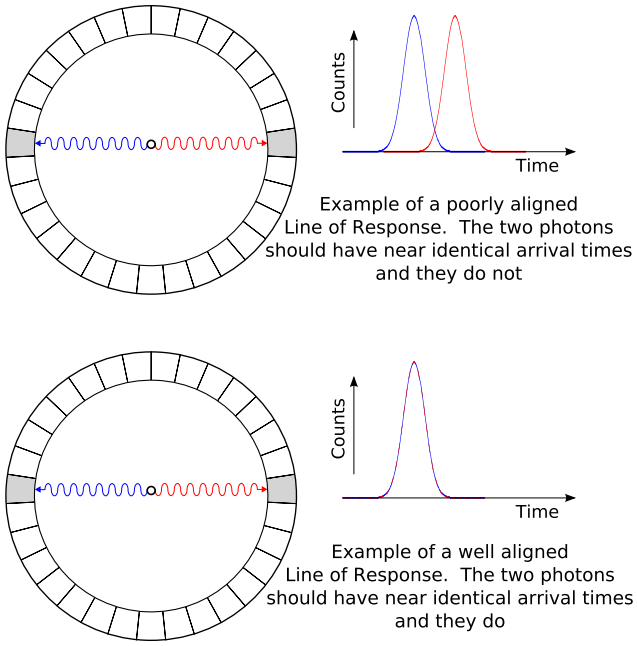

Figure 2–1: Example of a poorly aligned and a properly aligned Line of Response

schematic of true and random events). Several methods have been developed to achieve the timing alignment efficiently and accurately [50–53].

A common method used to calibrate PET scanners is very slow and inefficient. It is an iterative process where a positron source is placed in the field of view and the count rate for each detector pair is maximized by adjusting the time offset (figure 2–2). Clearly having to do this for each detector pair is very time consuming and not entirely accurate. The other problem is that the adjustments to the time offset are done blindly, there is, initially, no indication of whether there needs to be more or less offset nor how much offset may be needed. While this method has many drawbacks which cause the timing alignment to be done very

rarely in a clinic, it does have the advantage of having very little dependence on placement of the calibration source [51].

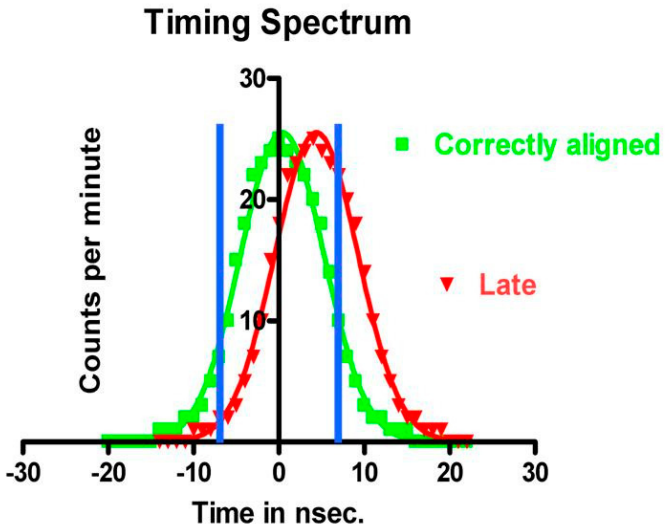

Figure 2–2: Schematic of the changing number of counts caused by time alignment with the timing window in blue

A method was proposed to use the orbiting transmission source to perform the timing calibration [51]. This method is intended to do an automatic adjustment of the time offsets. For each LOR the timing difference is calculated by orbiting the source around the ring of detectors and measuring the timing difference. The position of the orbiting source will cause time of flight differences between the detectors in the lines of response, but this is taken into account by averaging the differences of when the source is across from each detector (see figure 2–3). The timing difference values for each set of detectors in each LOR in a perfectly aligned scanner would be identical, and the goal of this method is to achieve that.

From the table of offsets, an average is calculated and the detectors are adjusted automatically to achieve a time difference in each LOR close to the average. These steps are repeated multiple times to complete the method (usually three or four iterations will do).

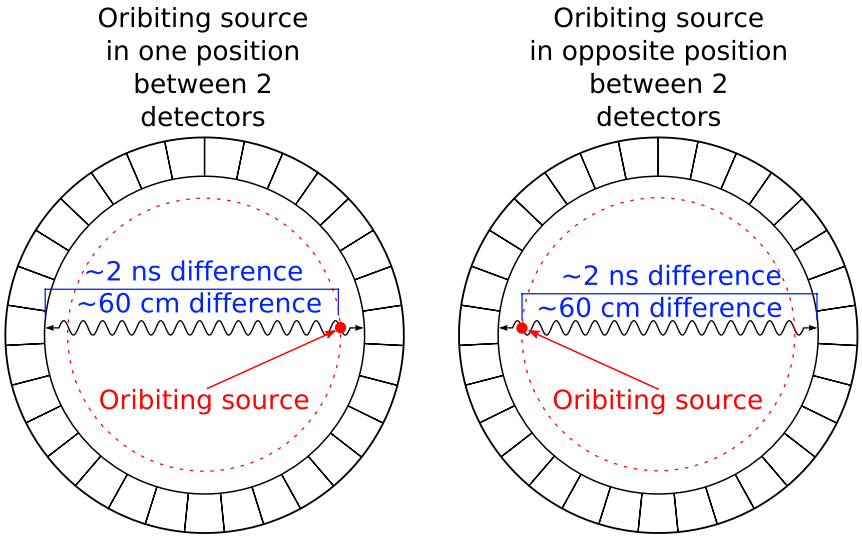

Figure 2–3: Position and time difference of a transmission source

A method similar to the one above was developed in 2002 to do the time calibration on the CPS high resolution research tomograph (HRRT) [53]. This method could be applied to any PET scanner who's electronics have the same capabilities as the HRRT. The motivation for this method was the use the narrower coincidence window that is provided by the HRRT (10 ns down to 6 ns) in order to reduce randoms 40%. In this scanner there are two methods that can be used to adjust the time offset; the first is to change the value that is output by the time-to-digital converter (TDC), but this only has a course adjustment of 2 ns. The other option is to adjust the constant fraction discriminator (CFD)

delay (see chapter 3.1 for a full description of both CFDs and TACs). The group found this lead to adjustments of about 200 ps. Since there is one CFD per block, only the offsets of each block may be changed, not the offset of each crystal. Using an orbiting rod source (orbit radius of 10 cm) data is taken for 10 minutes and the time differences from each block to all others are histogrammed. Based on these histgrams the CFD delay was adjusted accordingly. It was found that four iterations were usually required to obtain the best alignment. The resolution of the scanner was minimized to 2.82 ns; more then adquate to lower the timing window to 6 ns.

In recent years new scintillators have been developed, one of the most popular crystals is LSO: lutetium oxyorthosilicate [54]. The stable isotope of lutetium is Lu-175, but Lu-176 is also common in lutetium sources. Lu-176 is radioactive, emitting 595.8 keV electrons and a photon sum energy of 597 keV. The abundance of the radioactive isotope is 2.6% naturally, it also has a very long half life of 4.05×10^{10} years [55]. A recent appraoch to performing the PET time alignment is to take advantage of this radioactivity. When Lu-176 decays a electron is released into the medium, in this case, the LSO, the energy from the electron will cause a light flash in the scintillator and a signal to the electronics. Once the electron is released the nucleaus is in a metastable state and promptly ejects a photon cascade with an energy sum of 597 keV. This energy may be detected by another detector in the ring and will generate a timing signal. A series of signals will be generated from each detector to another, creating a table of differences. The time offset for the emitting detector is adjusted once many counts are taken and

the timing information well known. This is performed for each detector in the scanner [52]. The advantage of this system is the radioactivity is intrinsic in the scanner, but this has the flaw of needing radioactive scintillatorsand the low count rate from LSO increases the time needed for the alignment.

The problem with each of these methods is the lack of a single and constant reference, so each is done in reference to different signals. The use of just one reference for each detector would be very useful. A timing probe consisting of a positron source, a scintillator and a PMT was developed to address this problem [56–59]. The scintillator used is a plastic scintillator, Polyvinyl toluene (PVT), which is low density, low Z but is very fast. The scintillator is machined into a small cylinder, cut in half, the center is hollowed out and a positron emitting isotope is inserted. The scintillator is glued back together and optically coupled to a fast PMT. This is all housed in a light-sealed container. The probe is put in the center of the PET scanner and connected to the coincidence circuit (figure 2–4).

The radioisotope releases a positron into the plastic scintillator causing a light flash that is converted to an electrical signal by the PMT and sent to the electronics. When the positron has lost its energy it annihilates and gives off two 511 keV photons. It is not necessary for each photon to reach a detector since the coincidence is made to be between the timing probe and any detector. Since each pair of photons must have a positron emission, there will often be a coincidence when one photon is detected. The low density and low Z of the plastic scintillator gives it a low probability of attenuating the annihilation photons, which

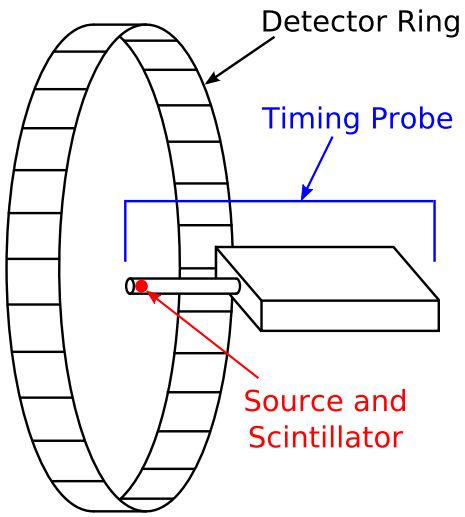

Figure 2–4: Placement of the timing probe in the ring of detectors

is desirable so that as many events as possible happen in the scanner's detectors. With the probe in the center of the ring of detectors the time of flight from the probe to each detector is the same, because of this and the unchanging processing time from the probe, a constant and identical source is given to calibrate each detector offset.

2.2 Time Drift and Stability

If the timing alignment could be performed once and it was not needed again, this would be ideal. Even if this was to be done after installation, the time could be taken as part of the setup of the scanner. Unfortunately this is not the case and the equipment exhibits time drift; losing its alignment.

Timing drift occurs because of many factors. Changing out a component is one obvious reason for time drift. New components that have replaced old components will very likely exhibit different timing characteristics. As mentioned

in the previous section, the crystals, PMTs and electronics may all cause a change in the desired time offset. When components are replaced the timing calibration should be performed again to compensate for likely differences. As well, change in timing can occur if one cable is simply replaced by another cable of different length. In a 50 Ohm cable a signal travels 19 cm in 1 ns, so significant differences can occur with small cable length differences [60].

As components age they also show a change in their properties [38,61]. These changes can also result in time drift. Although the changes are gradual enough to not require daily or even weekly calibration there is evidence that calibrating at least twice a year would be useful [61,62]. Since each block detector is at end of a LOR there is an interdependence of the timing stability on each individual block detector; therefore the stability of the alignment of the entire scanner is dependent on the least stable of the detectors. Although each PMT is tested by the company before installation it has been shown that there is great variation in the stability of detectors [61].

Another factor believed to cause time drift and misalignment is the temperature variation [63]. Not only can detectors in a scanner have a different temperature from each other, they may respond differently to a change in temperature. The count rate of a system increases with temperature as does the activity calibration factor; these differences show a change in detector response to temperature and suggest that it is likely the temperature could have an effect on the timing properties. Although it is likely that there will be some timing difference

based on temperature, there is evidence that this may not be true within a small temperature range($\pm 2^{\circ}$ C) [62].

2.3 Time Resolution

Time resolution is the measure of detector's ability to accurately record the time of an event. The better the time resolution is the more accurately the event is time stamped. The better the resolution is in a PET scanner the better the likelihood of having a narrower timing coincidence window. The resolution of a detector is dependent on several properties. The primary scintillator property that has an effect on the time resolution is the decay time. The scintillation process involves the interaction of a high energy photon moving orbital electron to a higher energy state. When the electron moves back to the lower energy state the low energy photons are ejected (see figure 2–5). The time is takes for the electrons to excite and de-excite to complete is known as the decay time [6]. The generally accepted shape of a scintillation pulse is given in equation 2.1; where τ is the population of the optical levels and τ_1 is the de-excitation of the levels [27, 64]. There are two advantages to a fast decay time; one is an improved time resolution and the other is a decreased deadtime, leading to an increased sensitivity to higher count rates.

$$I = I_0 \left[\exp(\frac{-t}{\tau}) - \exp(\frac{-t}{\tau_1}) \right] \tag{2.1}$$

Although generally thought of as factors influencing the energy resolution, the geometry and light output of the scintillator also have an impact on the time resolution [49, 65]. The geometry and light output both impact how much

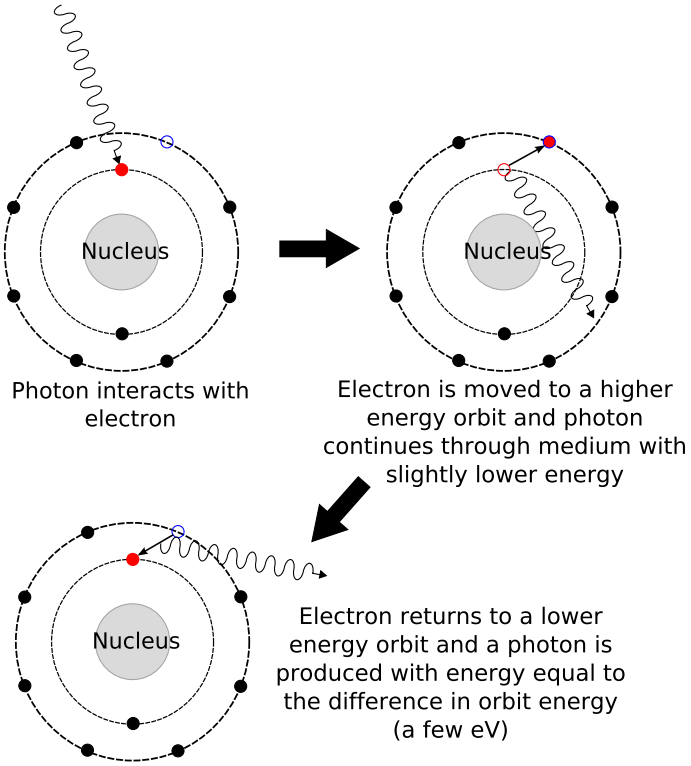

Figure 2–5: Process of scintillation, the time this takes for all atoms is the decay time

light reaches the PMT. Small differences in the chemistry of the crystal may be responsible for changes in light output between crystals made at different times. The larger the crystal is the more light it outputs. This is simply because the photons have more interactions in the crystal if it is large. Also, if a crystal is not polished there is an increase in light loss and decrease in sensitivity [66].

The transit time spread (TTS) is an evaluation of a photomultiplier tube's ability to resolve time differences [67, 68]. The shorter the TTS is the better the time information will be resolved. The non-zero TTS results in a loss of resolution in the time stamp of the scintillation. Transit time spread is a measure of the pulse arrival time difference of a large number of pulses (at least 50,000). The FWHM of the curve created (which will not be unlike that in figure 1–7) is the transit time spread for a PMT.

In order to process scintillation events a constant fraction discriminator (CFD) is required. One parameter of a CFD is the walk time, which essentially evaluates its ability to accurately process the time information. The larger the walk time is the worse the resolution of the signal will be. The CFD is designed to preserve timing information as well as possible, but the ability to do so to the extent required by the application varies.

The time information is digitized by a time to amplitude converter (TAC). This equipment takes a start signal, and some time later, a stop signal and outputs a square wave with amplitude which is linearly proportional to the time difference between the start and stop signal. The ability of the TAC to produce a square

wave of constant amplitude when there is a constant time difference has an influence on the time resolution.

2.4 Time of Flight PET

Time of flight PET was first investigated in the early 1980's [68, 69]. Early time of flight (TOF) scanners were made using Cesium Fluoride (CsF) and later Barium Fluoride (BaF_2) and modern TOF scanners use LSO (or LYSO) as the scintillator [70–72]. In order to have the best time resolution possible, it is necessary for a scintillator to have a short decay time, this is the common characteristic amongst all TOF scintillators.

Scintillator	CsF	BaF_2	LSO
Decay Time (ns)	5	0.6 - 0.8	40
Z_{eff}	52	56	66
Density $\left(\frac{g}{cm^3}\right)$	4.6	4.9	7.4

Table 2–1: Time of flight scintillator properties [9, 68]

Time of flight PET takes advantage of the difference in arrival times of two photons from the same annihilation to infer spatial information of the annihilation [68]. If aligned properly, a detected coincidence between two crystals will have a time difference for any annihilation event that does not occur at the midpoint between the detectors, this time difference is used to place the position of the event (see figure 2–6). Since the time resolution of the system is

imperfect, the precise spatial position can not be obtained from time offsets but instead, a probability is used to place the likelihood of the event (see figure 2–7).

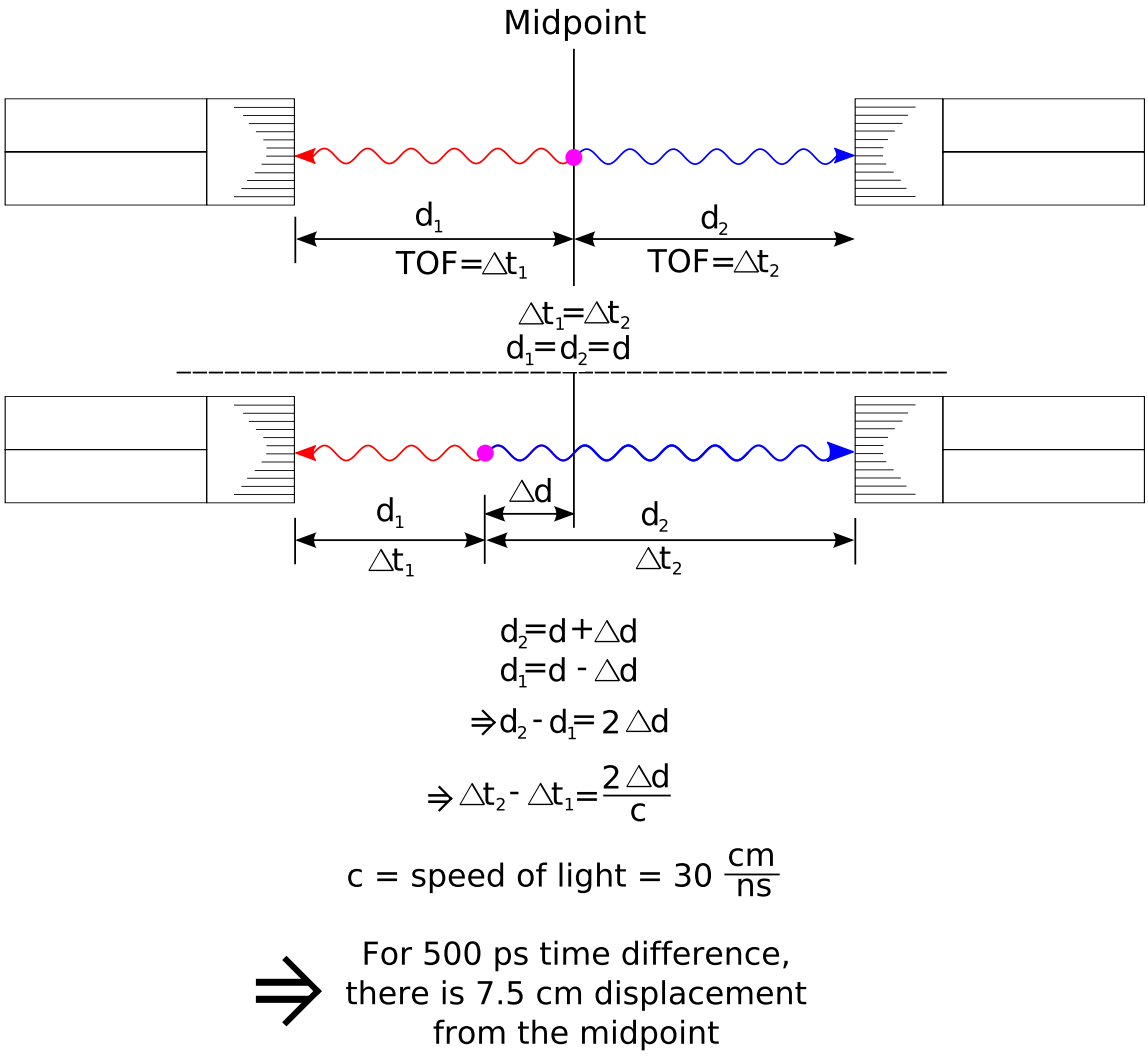

Figure 2–6: How time of flight information becomes positional information [68]

If the time resolution of the scanner were zero the event could be placed with absolute precision and this would increase the spatial resolution. In that case the advantage to TOFPET would be a lack of a need for reconstruction and less

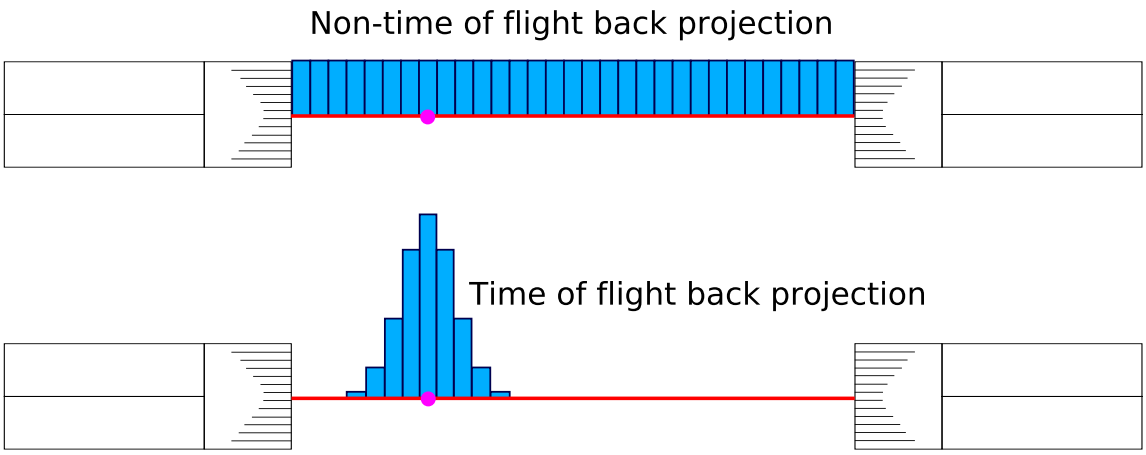

Figure 2–7: **Top:** With a non-time of flight scanner the event (purple) is given equal probability (blue bars) along the entire line of response (red). **Bottom:** With a time of flight scanner the probability of the event is skewed according to the difference of the arrival times and the time resolution of the scanner.

blur [68,73]. Since that is not the case and the time resolution (and the associated localization spatial resolution) is non-zero, the advantages of time of flight scanners is an increased signal to noise ratio (for the same number of counts) and a reduced reconstruction time [73–79]. The relation of the time spread to the spatial spread is [75]:

$$\Delta x = \frac{c\Delta t}{2} \tag{2.2}$$

Initially time of flight PET was abandoned due to a lack of suitable scintillators and troubles with the stability of the electronics.. As previously described, the scintillator for a TOF scanner must have a very fast decay time. If this is not the case the time resolution will not be narrow enough to accurately locate the event. Since the advantage of TOF in the image is an increased signal to noise ratio (SNR) the same images can be obtained with conventional PET with an

increased number of counts. In early TOF scanners the fast scintillators had a low sensitivity and when new scintillators (mainly BGO) were developed with much higher sensitivity but a long decay time, TOF was abandoned for conventional PET. The improved sensitivity of BGO produced better SNR without TOF then BaF_2 and CsF did using time of flight. The electronics of TOF scanners also had to be much more stable then those of conventional PET creating more reasons to abandon this technique. As electronics technology advanced and new scintillators were developed (mainly LSO/LYSO) that combined a high sensitivity with fast decay times, TOFPET was once again advantageous.

The theory behind the reduction to the noise in a TOFPET image is relatively simple. For any coincidence there is a probability of the spatial placement of the event associated with it. Through filtered backprojection this probability results in a reduction in the incrementing of the pixels from where the annihilation did not occur (as shown in figure 2–7). This same consequence will occur for the statistical noise. Using TOFPET to place the annihilation will result in the noise contributing to fewer pixels, but the real data remaining intact. The reduction factor of noise in TOFPET is [75–77, 80]:

$$f = \frac{2D}{c\Delta t} \tag{2.3}$$

where D is the size of the emission source, c is the speed of light and Δt is the time resolution. The SNR ratio of TOFPET to conventional PET is $\sqrt{f}$. Equation 2.3 shows that the improvement of TOFPET over conventional PET is not only dependent on the time resolution, but also the size of the radioisotope distribution.

Since the size is a factor in the gain, the size of the patient is also important, and TOFPET shows a larger improvement for larger patients. Also, body scans show more improvement then brain scans.

What is hidden in equation 2.3 is that each of the event types will show different gains from TOFPET (see figure 1–5 for the event types). The effective size of the scatter and random counts will be much larger then the size of the true counts, this will result in an even larger reduction of the degradation of the image from the contribution of scatter and randoms. Equation 2.3 assumes that $f_{true} = f_{random} = f_{scatter} = f$, when, in reality, these are different and the gain from TOFPET has been underestimated [76, 78, 81].

Another advantage of TOFPET is the ability to have a relatively simple simultaneous transmission and emission scan [73]. Since 15 cm is approximately the separation between the transmission source and the patient, a 1 ns time resolution would enable the electronics to decode the transmission counts from the emission counts. One disadvantage of using this method is dramatically increasing the dead time of the near detector and, thus, having a time dependent sensitivity. The ability to do the transmission and emission scan would significantly decrease the total scan time per patient.

Since time of flight PET relies heavily on the best scanner time resolution possible, the time alignment becomes very important. A misalignment of just 1 ns (which is common, as seen in the HRRT example) will cause a spatial misplacement of 15 cm (see figure 2–8). A systematic 15 cm misplacement of an event will result in a large amount of blurring in a PET scan. If this 15 cm

Time Resolution	Distribution Size (cm)	SNR Improvement
3 ns	10	0.47
	20	0.67
	30	0.82
2 ns	10	0.58
	20	0.82
	30	1.00
1 ns	10	0.82
	20	1.15
	30	1.41
650 ps	10	1.01
	20	1.63
	30	2.00
500 ps	10	1.15
	20	1.43
	30	1.75
250 ps	10	1.63
	20	2.31
	30	2.83

Table 2–2: Improvement in SNR for various time resolutions and distribution sizes using equation 2.3. SNR improvement below one does not imply that there is a disadvantage to using TOF at these resolutions and sizes, just that there is no longer any advantage (beyond reduced scatter and randoms). Note that the Philips Gemini TF TOFPET scanner has a reported time resolution of 650 ps [82]

misplacement happened during simultaneous transmission/emission scan events from the transmission source may be mistaken for events from the injected radiopharmaceutical. Time alignment is important in conventional PET to reduce the number of random counts present in the data, but the alignment become critical once using TOFPET to accurately place the events.

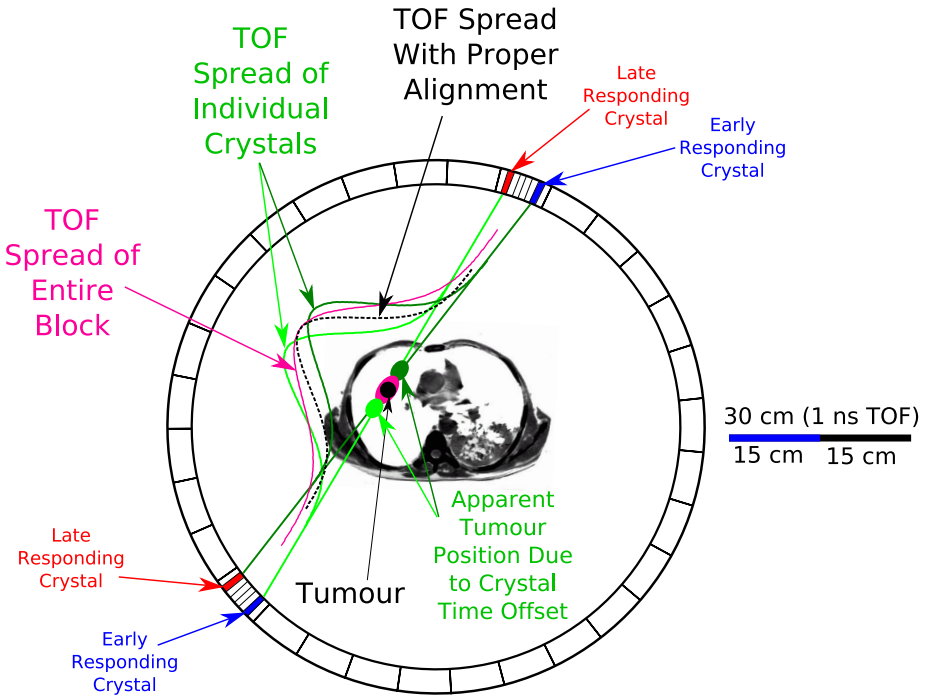

Figure 2–8: Example of data misplacement due to 1 ns time misalignment

CHAPTER 3
Equipment and Methods for the Measure of Time Resolution and Energy Spectra

3.1 Equipment

Once the high energy photons are converted to low energy photons by the scintillator and the PMT has converted the low energy photons to an electrical pulse, this pulse needs to be processed to infer some information from it. The energy and time information about the initial photon can be obtained from the pulse. In my experimental setup the equipment used was a constant fraction discriminator (CFD), a time to amplitude converter (TAC), a summing amplifier, a timing amplifier, an integrator, an analogue to digital convector (ADC) and a multichannel analyzer (MCA).

3.1.1 Constant Fraction Discriminator

In the results I present, the lower level discriminator (LLD) is used to decrease the noise and scatter that is present in the signal. In a PET scanner the LLD is used for that purpose, but also for its lower limit on the energy window. The simplest method to discriminate simply rejects any pulses that are below the threshold voltage and accepts any above it [27]. This is done by reading the height of the leading edge; once the threshold is surpassed the pulse is accepted. This method works well when the dynamic range of the pulses are small, but it will cause timing errors if there is a large time jitter, different shaped pulses, or, most

importantly in these experiments, a large range of amplitudes with similar rise times (see figure 3–1). If timing information is not important, this method will perform acceptably under many circumstances.

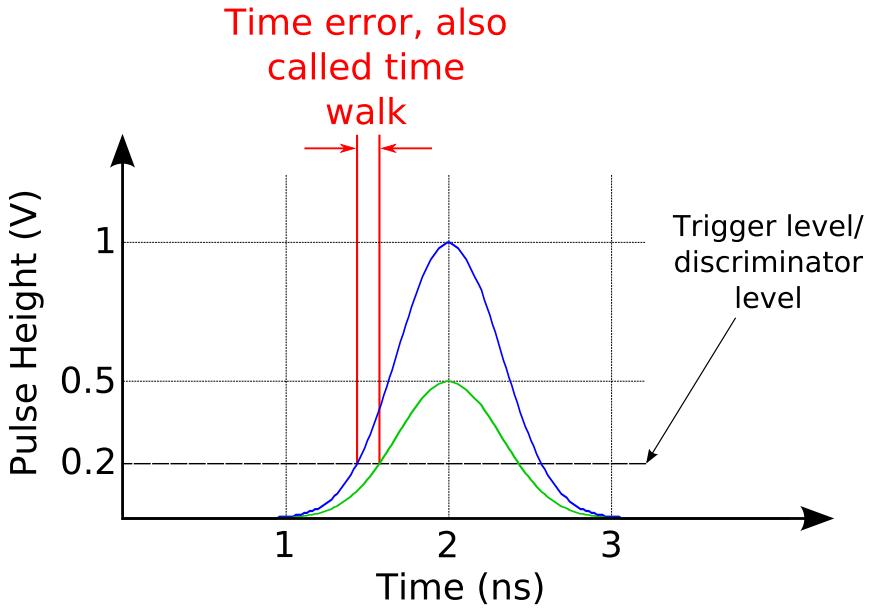

Figure 3–1: Time walk example for two pulses with the same rise time but different amplitudes

In PET scanners the timing information is very important. It is used to determine coincidence events as well as to reduce random counts and is critical in time of flight PET. Systematic errors caused by time walk must be eliminated as much as possible in these applications. In order to enable discrimination but keep the timing information intact a constant fraction discriminator (CFD) is used [27]. The input signal goes to the CFD and the electronics split the signal into two; one of the signals is attenuated (usually 80%, sometimes 60%), the other signal is inverted and delayed. The delay should be adjustable but is ideally longer

than the 10% to 90% rise time. The exact length of the delay should be found experimentally, but a starting point is:

$$t_{delay} = t_r(1 - f) \text{ ns} \tag{3.1}$$

where t_{delay} is the time of the delay (in ns), t_r is the rise time of the signal (in ns) and f is the fraction the signal is multiplied by (usually 0.2) [60]. The delays are often done by running the signal through a 50 Ω cable. If this is the case, the signal will be delayed 1 ns for every 19 cm of cable length. Once one signal is truncated and the other is inverted and delayed they are summed. A signal is output from the CFD when the summed signal crosses 0 V (x-asis)(see figure 3–2).

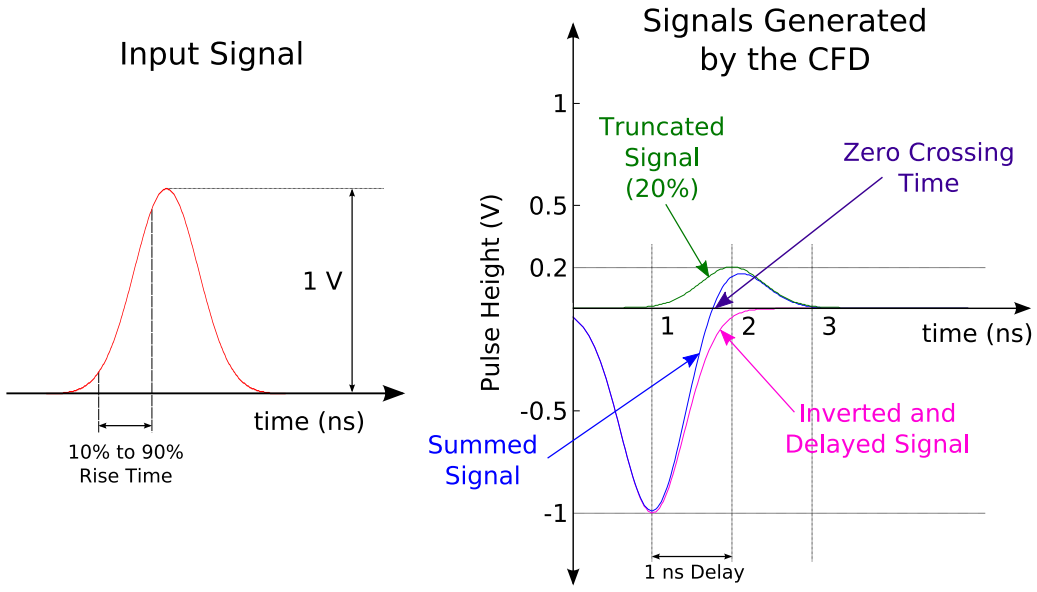

Figure 3–2: Example of CFD processing on a Gaussian signal with 0.4 ns standard deviation, 1 V height, and 0.676 ns rise time. The CFD uses a fraction of 20% and a 1 ns delay has been applied. The CFD will output a pulse at the time of the zero crossing.

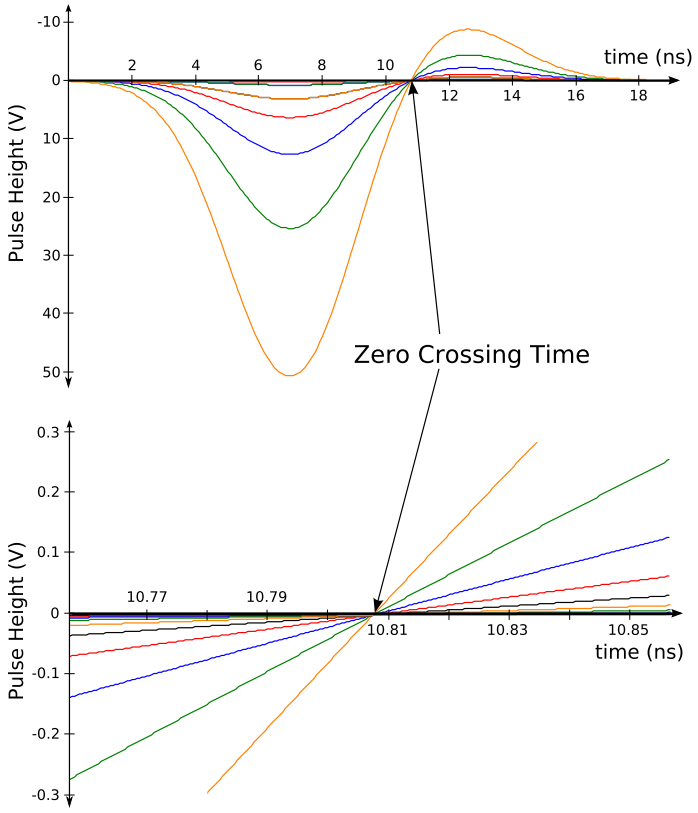

Figure 3–3: Example of the zero crossover for 10 Gaussians with the same rise time (3.38 ns) but amplitudes from 0.1 V to 51.2 V. The height of the Gaussian is doubled for each subsequent input. The delay in the inverted signal is 5 ns. Note that each of the curves has the same zero crossover point so the CFD would output a signal at the same time, thus preserving the timing information. The top image is the entire CFD signal, the bottom image is zoomed in on the zero crossover point.

In order to compensate for differences in input signal shape, CFDs come with a walk setting. Some CFDs (such as the Ortec CF8000 oct CFD) adjust this automatically, others can be adjusted manually. The walk time adjustment is used to align the zero crossing point of all the different input pulses. Since the CFD must be able to function for many different shaped input pulses, it can not be optimized for all of them. Using the walk time adjustment provides that opportunity. Time walk is also a parameter used to evaluate the performance of a CFD. The shorter or smaller the time walk (measured in ps) the better the timing information of the input is preserved.

Some CFDs also come with the option to shape the output pulse [60]. The Canberra 454 CFD allows the user to widen the pulse for other equipment to process.

3.1.2 Time to Amplitude Converter

A time to amplitude converter (TAC) is used to output a near square pulse with height proportional to the time difference between two signals. Each TAC will have a start and stop input. Each input will be a signal coming from the output of a constant fraction discriminator. When the start pulse arrives to the TAC a circuit is closed and a constant current is sent to a capacitor which is then charged [83, 84]. When the stop pulse arrives this current is stopped. Using equation 3.2, the voltage on the capacitor will be proportional to the time difference between the start and stop pulses. The voltage is then sent to an amplifier and onto a linear gate and stretcher (see [85] for the single NIM module version). The

stretcher reads the peak amplitude of the input pulse and outputs a square wave with amplitude equal to the peak height.

$$V = \frac{It}{C} \tag{3.2}$$

where I is the current, t is the time between the start and stop pulses and C is the capacitance.

The signal that will be sent to the stop input should be sent through a delay line (a cable used to delay the pulse) that is at least 190 cm (50 Ω cable) which is a 10 ns delay [83]. Part or all of this delay may be internal in the TAC. This delay is needed because the electronics and circuits of the TAC do not perform well at small time differences. This does not mean that the equipment can not be used to measure small differences. Rather, there will be an offset applied that will need to be subtracted for absolute differences if needed. The TAC used in these studies, the Canberra 2145, also includes a single channel analyzer (SCA) and a gating option, but these were not utilized. It has input and output monitors as well as other features [86]. An important adjustment can be made to the range of times that the TAC can encode. In the Canberra 2145 this range is from 5 ns to 1 ms.

Previous tests have shown some limitations of TACs with high input count rates and also with random events [87]. While this could drastically influence results, these consequences were not seen at the count rate and with the equipment used in my studies.

Other methods of converting time to an encoded electrical signal have been investigated and can be seen in [88–90].

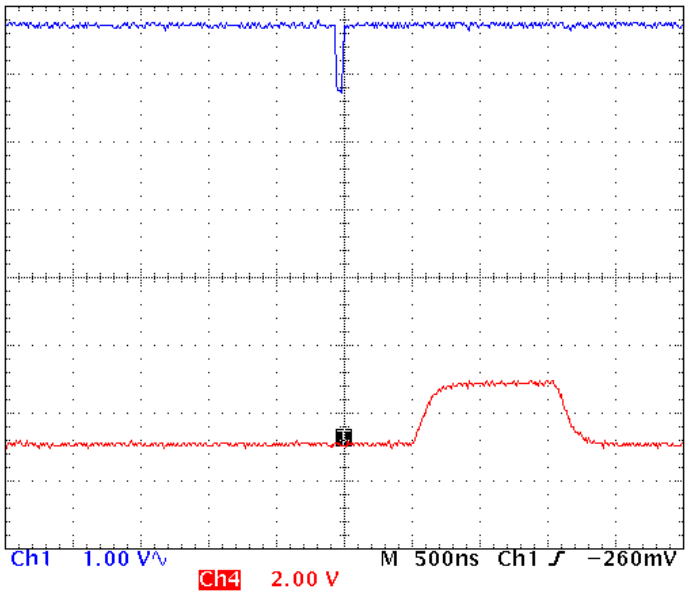

Figure 3–4: **Top/Blue:** Sample output from a CFD. The signal is about -1 V high. **Bottom/Red:** Sample output from a TAC. The signal is about 2 V high, but this is dependent on the time difference between two signals. The time scale is 0.50 μs/div.

3.1.3 Analogue to Digital Converter and Multi-channel Analyzer

An analogue to digital converter (ADC) is used to convert an analogue signal into a digital signal [91]. An analogue signal is continuous whereas a digital signal is discretized. The signals are digitized in order to be processed and stored by a computer or other electronics. The ADC will sample the analogue signal at a specified interval (usually given in Hertz (Hz) or times per second). At each sampling point the value of the analogue is converted to a digital binary number. The resolution or accuracy of the ADC is dependent on the number of bits the binary numbers are (usually 8, 10 or 12 bits) and the range of voltages the ADC is expected to input. For example, if the ADC is 10 bit and accepts a range from 0 to 5 volts, the ADC can discretize the signal with the following accuracy:

$$\text{Number of levels} = 2^{10} = 1024 \tag{3.3}$$

$$\frac{5\text{ V} - 0\text{ V}}{1024} = 4.88\text{ mV} \tag{3.4}$$

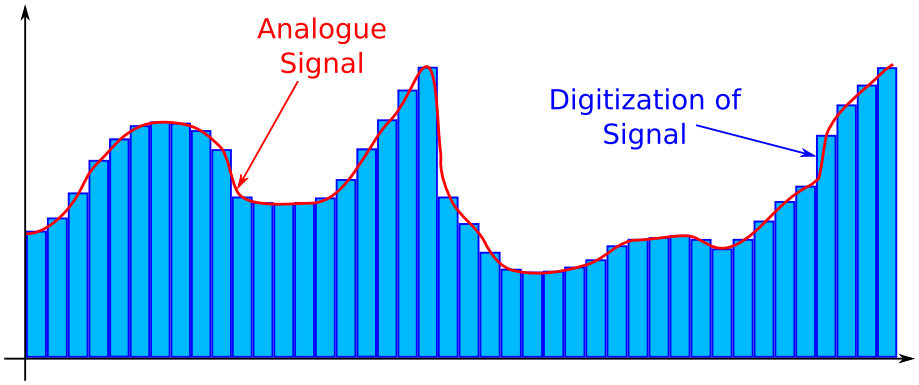

Figure 3–5: Example of an analogue signal being digitized. The analogue signal is sampled at the center of each bar.

There are two different primary methods for ADC design. The first, called a linear ramp converter (or Wilkinson type), is the most commonly used method [27]. This method is quite simple. When an input is detected the ADC starts charging a capacitor, once the peak of the signal is reached, the charging is stopped. Using a constant current, the capacitor is then discharged. While discharging, the a square wave oscillation signal is sent to a counter, once the capacitor has fully discharged the the counter stops counting. The number of counts on the counter (and the time taken to discharge the capacitor) is the digital representation of the voltage of the input signal.

The other method, which is less commonly used because it lacks linearity, is called the successive approximation method [27]. To detect the height of the signal the circuit continuously makes a comparison of the input pulse to the values the ADC can take as input. The input pulse will first be examined to see if it is in the lower portion or the upper portion of the ADC range. If in the upper half, the most significant bit in the address register becomes a 1, if it is in the lower half, the most significant bit becomes a 0. This is done for all the bits in the address register until all bits are a 1 or 0. The speed of conversion with this method is constant, where the Wilkinson method is variable: the larger the input the longer the conversion time.

The extension from an ADC to an MCA is is small one. The most significant addition to the ADC is memory to store all the values the ADC has obtained [27]. This memory stores each value from the ADC into a bin as a count. For example, if the ADC returns a value of 2.4 V, the memory will store that value in the

bin that 2.4 V falls into, such as all values from 2.395 V to 2.405 V. The MCA may also have a single-channel analyzer (SCA) to serve as an upper and lower discriminator before the pulse is input to the ADC.

3.2 Experiment Setup

3.2.1 Setup for Measuring the Time Spectrum of Single Crystals Optically Coupled to a Single PMT

In order to extract only time information from a single crystal coupled to a photomultiplier tube, the signal from the PMT is first sent to the constant fraction discriminator, then to the time to amplitude converter then to the multi-channel analyzer. The two signals used for the TAC start/stop come from a Scanwell Systems time alignment probe (as discussed in section 2.1 and in references [56–59]) and from the crystal/PMT. The Scanwell Systems probe is the reference time for all but one experiment. The probe gives a pulse when the positron is released and loses energy in the plastic scintillator. That signal is sent to one CFD then to the start input of the TAC. The stop signal is from the PMT/crystal once it is detects the 511 keV annihilation photon, run through CFD and a delay box. The output of the TAC is input into a MCA to record the pulse height and the data is imported to a PC for the analysis of the timing information and for pulse width/time resolution measuring. The one exception to using the time probe as the reference was when a crystal/PMT combination was used in place of the timing probe. When this was done the activity came from an external source placed between the two PMTs. This was only done with BaF_2 as the crystal. That experiment was done to set an absolute minimum for the time resolution of the system (since BaF_2 was the fastest scintillator we tested).

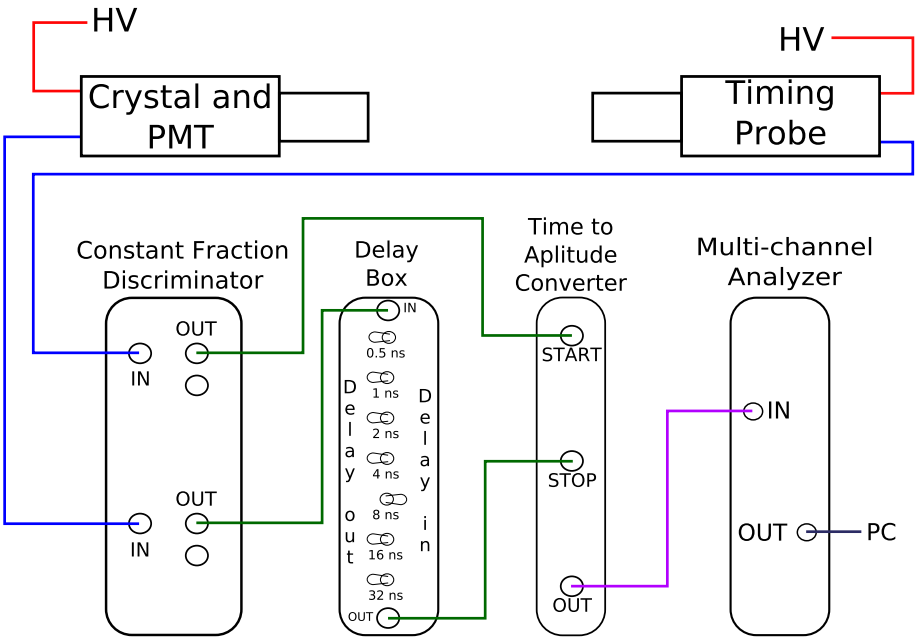

Figure 3–6: Experimental setup for extracting the time spectrum from a crystal/PMT combination in coincidence with the Scanwell Systems timing probe.

3.2.2 Setup for Measuring the Energy Spectrum of Single Crystals Optically Coupled to a Single PMT

When the desired information from the crystal/PMT setup is the energy spectrum, a change is made to the setup. The signal from the PMT is no longer sent to a CFD, rather to a signal integrator. The integrator integrates the signal, multiplies it by -1 and outputs that signal. That signal is sent to a ADC/MCA and the pulse height is stored. Depending on the performance of the ADC/MCA the signal may be passed through a signal stretcher before the MCA to ensure the peak height is digitized.

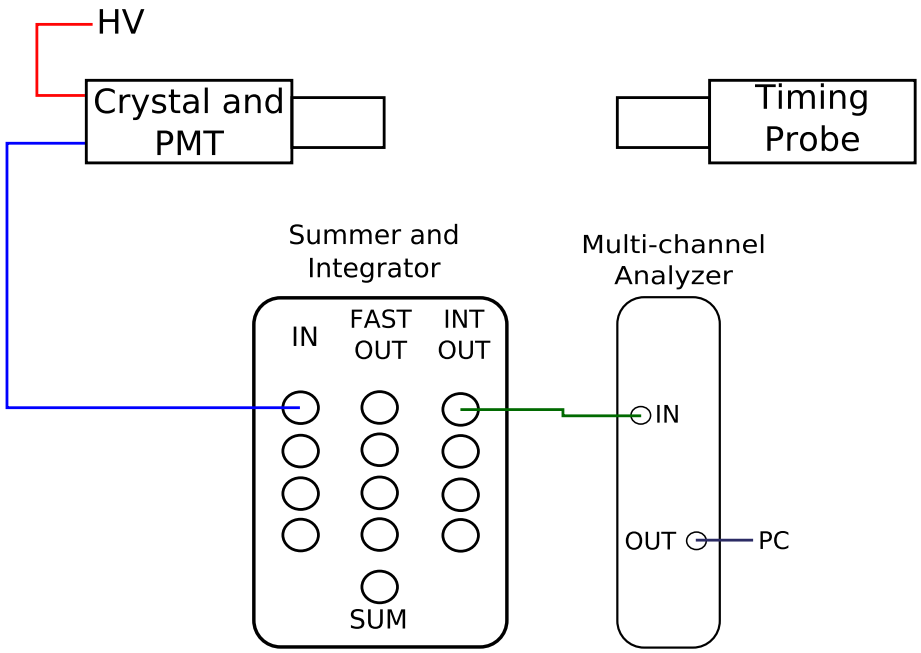

Figure 3–7: Experimental setup for extracting the energy spectrum from a crystal/PMT combination. Note that the timing probe is just used for the embedded activity (Sodium 22).

3.2.3 Setup for Measuring the Energy Spectrum and Time Spectrum of Block Detectors

A more complex experimental setup is needed when testing a commercial block detector and extracting both the time and energy information. This setup mimics much more closely what would be performed in an operating PET scanner. The signals from each of the four PMTs in the block are sent to a summing amplifier which was made by Nan Zhang, a former student of the same lab, and current employee of Siemens Molecular Imaging. The amplifier has one input for each PMT from the block and outputs the sum of the four signals as well as the integrated and positive signal for each. The summed output is sent to a CFD. From the CFD the signal is sent through a delay box and on to the TAC stop input. The start input is provided from the timing probe, as it was in section 3.2.1. The TAC outputs its time-encoded signal to an ADC. The integrated signals are sent to a timing amplifier (optional) and then input to an ADC. In order to operate the ADC two more inputs are needed. One input pulses to tell the ADC to record data, another input pulses to identify the information as the energy signal; the lack of this signal identifies the time data. The electronics used to deliver these pulses (simple logic pulses) were designed and built in-house. A second output from the CFD used by the block is sent to the ADC pulse producer to time the need for the identifying and ADC strobe pulse (figure 3–9).

The ADC is controlled and is data acquired by a DEC Alpha workstation running the open VMS operating system and software that was written in-house. This software controls the operation of the ADC and also stores the data appropriately. It should be noted that this setup is needed only for the extraction

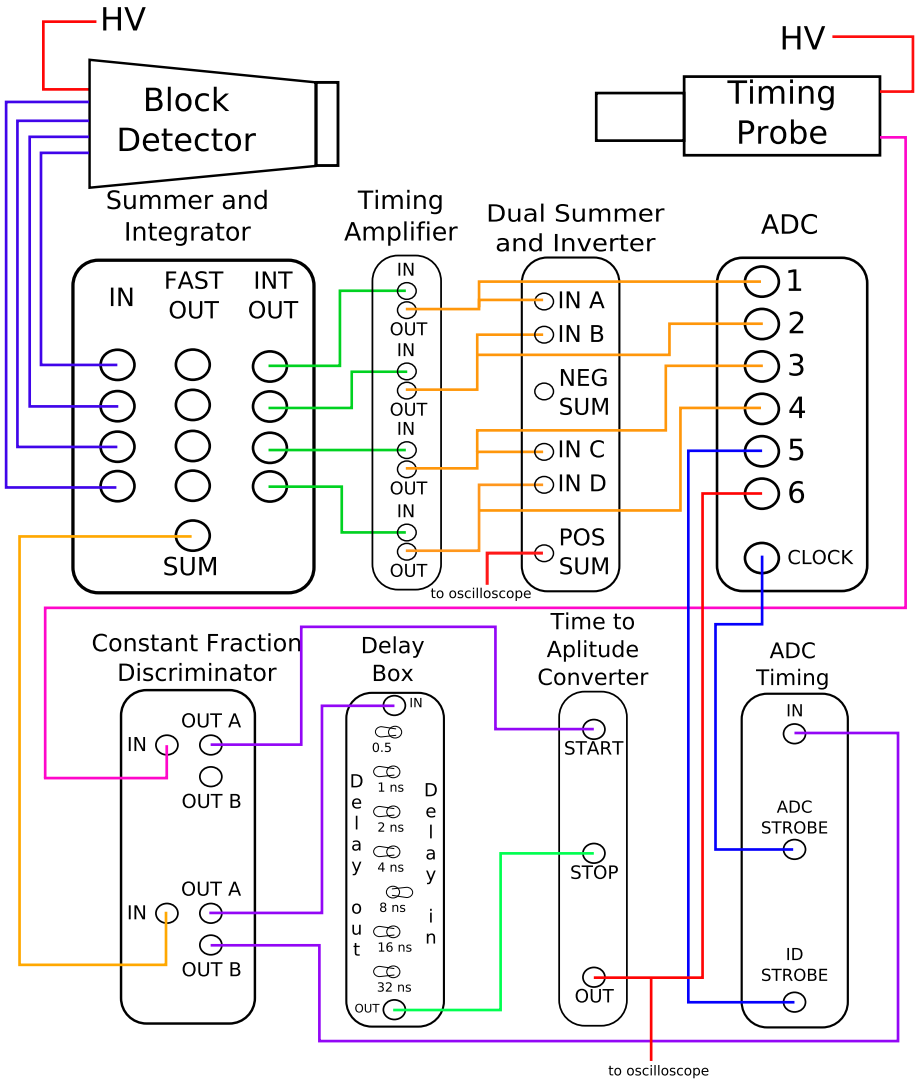

Figure 3–8: Setup when extracting both time and energy data from a commercial block detector. The ADC is controlled by software running on an Alpha 4/100 workstation.

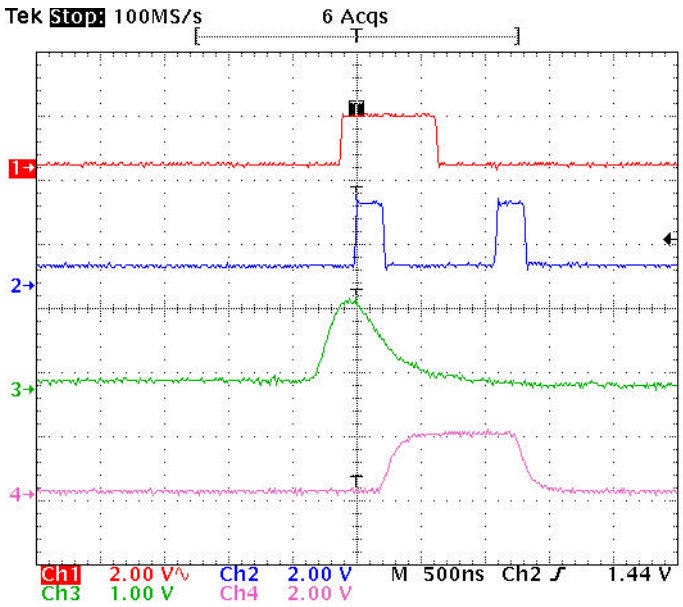

Figure 3–9: **Top/Red:** The ADC identification strobe, the pulse is placed so it is straddling the first ADC read strobe and will identify that data as the energy data. **Second/Blue:** The ADC read pulse consists of two square pulses, the first to read the energy pulse (**third/green**), this must be placed so the leading edge is as close as possible to the peak of the energy wave. The second pulse is placed so its leading edge is above the TAC signal (**bottom/purple**) and separated from the first read pulse by at least 1 μs. Here they are separated by a little more then 1 μs.

of time and energy data simultaneously. If these are not needed simultaneously the setup for the crystal/PMT combinations in subsections 3.2.1 and 3.2.2 are just as valid for the block detector with a small change. In order to extract solely the time information the signal for the four PMTs is summed then input into the CFD. For the energy data the signal for the four PMTs is integrated then summed and sent to the MCA; just one extra step for each.

3.3 Equipment, Software and Analysis Used

Initially a lower performance system was used starting with an old version of the timing probe. This timing probe had a PMT with a slower transit time spread and 10% the initial activity of the improved version which was the focus of these experiments. Aside from the timing probe, the CFD was also upgraded to improve the time resolution. On top of replacing the CFD the MCA was also replaced. This was not done for performance gain but because the initial MCA stopped functioning properly.

Once the experiment finished running the data was stored in the MCA, from there it was connected through a parallel port to a DEC Alpha open VMS workstation. The data was then transferred to a Windows XP PC for further processing.

The final results using an improved timing probe are the focus of these studies. The TAC was unchanged for these experiments, but the probe, the CFD and the MCA were all changed. The output of this MCA is directly into a Windows XP PC for processing.

Equipment		Properties
Timing Probe	PMT [92, 93]	Hamamatsu R1635 λ_{min}=300 nm, λ_{max}=650 nm, λ_{peak}=420 nm Borosilicate window 1.0×10^6 gain 869 ps TTS 8 dynodes 1250 V max
	Source [94–97]	Sodium 22 511 keV annihilation photons 1.2745 MeV decay photons 546 keV positrons 370 kBq (10 μCi)
	Scintillator [98]	Polyvinyl Toluene Cylinder: 7.92 mm high 8.62 to 9.15 mm diameter 2.5 ns decay time 423 nm peak emission 1.032 g/cm^3 density 1.58 index of refraction
CFD	Ortec CF8000 [99]	0 to -5 V input -10 mV to -1 V threshold 2, 4, 6, 8, 10 ns delays Auto walk adjustment $< \pm$250 ps walk
TAC/SCA	Canberra 2145 [86]	5 ns to 1 ms range Pulse width of 0.5, 1.0, 2.5 ns 250 ns Rise Time Time Res <0.01 % full scale+5 ps FWHM
MCA	Tracor Northern TN-7200 [100]	0 to 10 V input LLD $\rightarrow$ 0 to 100% of 8 V ULD $\rightarrow$ 5 to 125% of 8V 512 to 2048 channels

Table 3–1: List of initial equipment used for crystal/PMT timing experiments and their properties. LLD and ULD are acronyms for lower level discriminator and upper level discriminator, respectively. The CFD is a single width NIM module and the TAC is a double width NIM module [27].

Figure 3–10: Image of the older, lower performance timing probe.

Figure 3–11: New probe with a faster PMT and 10 times the activity of the old probe at manufacturing time (currently the activity is about 20 times higher because of the decay of the sources)

Equipment		Properties
Timing Probe	PMT [101]	Hamamatsu H6610 λ_{min}=160 nm, λ_{max}=650 nm, λ_{peak}=420 nm Synthetic Silica window 5.7×10^6 gain 160 ps TTS 10 dynodes -2500 V max
	Source [94–97]	Sodium 22 511 keV annihilation photons 1.2745 MeV decay photons 546 keV positrons 3.7 MBq (100 μCi)
	Scintillator [98]	Polyvinyl Toluene Cylinder: 7.92 mm high 8.62 to 9.15 mm diameter 2.5 ns decay time 423 nm peak emission 1.032 g/cm^3 density 1.58 index of refraction
CFD	Canberra 454 [60]	0 to -2.5 V input -5 mV to -1.0 V threshold External delay (0.6 ns internal) $< \pm100$ ps (typically $< \pm30$ ps) walk
MCA	Amptek 8000A [102]	0-10 V input Any LLD 256 to 16384 channels

Table 3–2: List of the final equipment used in the crystal/PMT timing experiments. The TAC has not changed.

Figure 3–12: The H6610 PMT that is used in the timing probe. Note that the H6610MOD PMT has the same attributes as the H6610 but runs on a positive HV instead of negative HV.

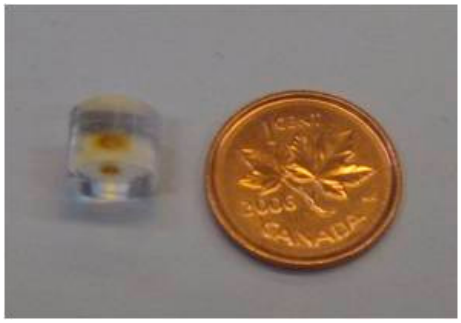

Figure 3–13: The source and scintillator used in the timing probe. The source is in the middle and can be seen as the brown spot.

When doing energy experiments on the crystal/PMT, only the MCA and the in-house amplifier are used. The MCA used is the same as the ones mentioned above. All results shown for the new probe are using the new MCA; however, it should be noted that there was no difference seen in the two MCAs.

When testing the block detectors an MCA was no longer used and a software controlled ADC replaced it. The ADC has 6 channels allowing it to record the data from each PMT individually as well as the timing information and an identification pulse. A Jorway Aurora-14 6 channel, 128k-word, 1 MHz, single width CAMAC module ADC was used [103].

When using the TN-7200 MCA, the data was exported to a PC for analysis. The software used was graphpad prism [104] which allows for plotting of data on an x-y axis and also has pre-made fitting functions and custom fitting functions. The data was fit to a sum of 3 Gaussians and returned the fitting parameters $A_1, A_2, A_3, \overline{x}_1, \overline{x}_2, \overline{x}_3, \sigma_1, \sigma_2$ and σ_3.

$$f(x) = A_1 \exp(-\frac{(x-\overline{x}_1)^2}{2\sigma_1^2}) + A_2 \exp(-\frac{(x-\overline{x}_2)^2}{2\sigma_2^2}) + A_3 \exp(-\frac{(x-\overline{x}_3)^2}{2\sigma_3^2}) \qquad (3.5)$$

To find the full-width-half-maximum (FWHM) of the data, the fitting parameters were input into a C program which created the function in memory and searched for the half maximum values and reported those in both channels and time (ns). The conversion from channels to time was done with the use of a delay box. The calibration is simple: the delay box provides a delay in a signal with the use of proper length of cables. The delay box used in these experiments

provides delays of 0.5 ns, 1 ns, 2 ns, 4 ns, 8 ns, 16 ns and 32 ns as well as any combination of those. To calibrate, the timing data is taken once, then again with the TAC stop signal delayed by a known amount (thus separating the peak by that amount of time). Once the experiment has run, the peak channel from both experiments is found with nearest neighbour interpolation, assuming symmetry of the peak. This information gives you the amount of time per channel on the MCA. The accuracy of the delay box was tested and confirmed against all the other delays and by moving the source and detector 30 cm/1 ns apart. Once the Amptek 8000A was used as the MCA, the data was no longer fit to the function as the software that came with the MCA found the FWHM when given the range to search for a peak. Also, the software allowed the channels to be converted to time with the proper calibration. The values found by this software were confirmed against the values found with the fit and were in agreement.

To calibrate the energy signals, the channel of the peaks are found and compared to an isotope table to find what energies the peaks occur at.

There were three block detectors tested in these studies: a Siemens HR+ detector (from the Siemens/CTI ECAT EXACT HR+ scanner [6]), the Siemens HiRez detector and the Siemens focus detector from the Siemens microPET Focus 120 and 220 small animal scanner. The HR+ detector consists of an 8×8 array of BGO crystals which are 4.05×4.39×30 mm^3 and coupled to four PMTs [105, 106]. The HiRez detector consists of a 13×13 array of LSO crystals which are 4.0×4.0×20 mm^3 [107, 108] optically coupled to four PMTs. The final detector is from the microPET focus line of small animal scanners from Siemens.

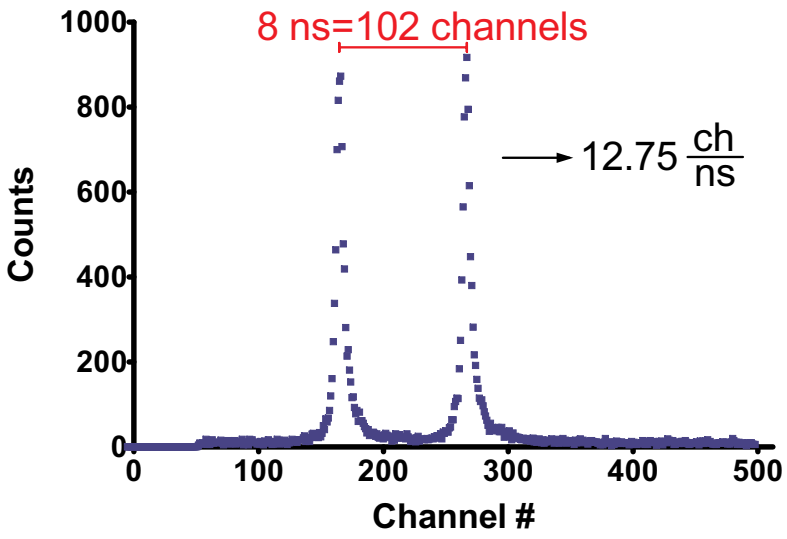

Figure 3–14: Example of the calibration to convert channels to time

These detectors are 1.51×1.51×10 mm^3 in a 12×12 array [109]. Each set of 144 crystals is optically coupled to a single position sensitive Hamamatsu R5900-C12 PMT [109, 110].

A series of software was developed in-house to run on the open VMS workstation that controls the ADC acquisition parameters, the energy discrimination window and the time discrimination window. While acquiring the data is stored with positional information and the time it is detected along with it's energy. Once the data is acquired more software allows the user to select individual crystal regions to see each energy spectrum for each crystal. There is also the ability to rescale the energy spectrum so that each crystal has its 511 keV peak in the same channel in order to decrease blur. The user can provide a range of channels, within

which the peaks are found by the software. Regions of interest can also be selected to plot and fit the time spectrum, outputting the time of arrival and the FWHM of each region, also useful if concentrating on each crystal. The obvious extension to this is to employ different time offset for shifted timing peaks to each crystal.

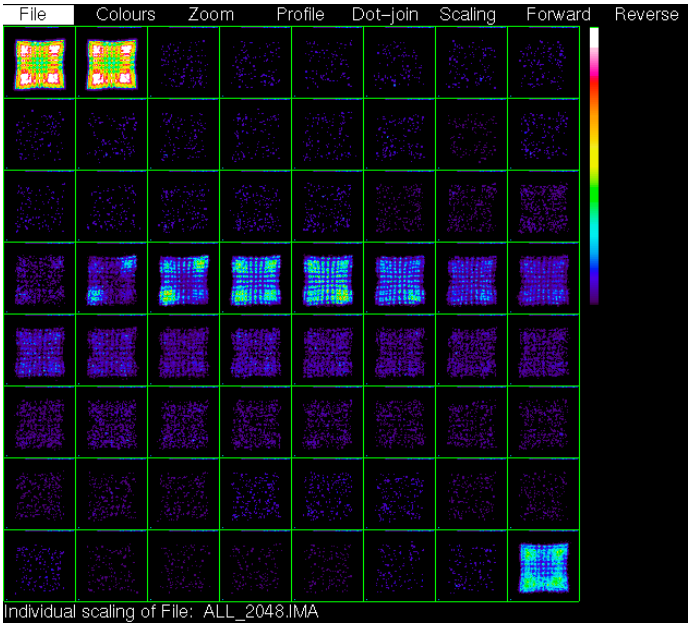

Figure 3–15: Sample of the image output from the software used with the block detectors. From this initial image/acquisition there is more analysis that can be done, such as selecting each individual crystal to observe the differences between each crystal. The first image is the sum of all the accepted events (in the energy and time window), the second image is the sum of all images that came before the time window and the last images are all images that came after the time window. All other images are the accepted images, they are binned by time. The amount of time in each image is the number of images (61) divided by the width of the time window.

CHAPTER 4
Results

4.1 Comparison and Time Resolution Results of the Old and New Probe and the Upgraded CFD

Initially, the experiments were done using the old probe and with either the block detectors or with the R1635 PMT coupled to the crystals that were already in the lab. While these experiments were being performed, the parts for the new probe had been ordered as well as new crystals. Each experiment optimized the parameters (threshold and delay) by first testing the time resolution as a function of the threshold then testing the time resolution as a function of the CFD delay by using the optimal threshold. The ideal settings were chosen by considering the resolution as well as the count rate.

Once these experiments were completed the new crystals and the components for the new probe had arrived. The new probe was built and tested, but it quickly became obvious that an upgrade in the CFD was needed. The absolute maximum that we were hoping to obtain was in the range of 212 ps for two BaF_2 crystals in coincidence. The value of 212 ps came from a paper by Bill Moses in which he went through each of the components of a commercial PET scanner and replaced them with high performance versions to see what the best achievable time resolutions are and to see what components are most responsible for the differences [49].

Crystal/ Detector	Timing Probe CFD Delay (ns)	Detector CFD Delay (ns)	Detector Threshold (-mV)	Calibration (ch/ns)	FWHM (ns)
LSO	6	2	2.3	12.3	1.0
Plastic (PVT)	10	6	60.0	12.4	0.76
HiRez	6	4	2.4	6.4	0.94
HR+	4	6	2.3	6.3	3.6

Table 4–1: List of parameters and results with the old probe and Ortec CF8000 CFD. The LSO and PVT were optically coupled to a Hamamatsu R1635 PMT. The CFD threshold on the timing probe was -40.0 mV for each experiment. The timing probe and PMT were run at -1000 V, the HiRez detector at +1000 V and the HR+ at +1500 V

Crystal/ Detector	Timing Probe CFD Delay (ns)	Timing Probe Threshold (-mV)	Detector CFD Delay (ns)	Detector Threshold (-mV)	Calibration (ch/ns)	FWHM (ns)
LSO	2	15.3	2	150.0	12.77	0.91
PVT	4	-2.0	6	100.0	12.62	0.59
BaF_2	8	-40.0	6	50.1	12.70	0.52
BaF_2/ BaF_2	-	-	6	31.4	12.75	0.594

Table 4–2: Time resolutions of the new probe using the Canberra 454 CFD. In the first three experiments the probe was operated at -1750 V. The LSO and PVT were coupled to the Hamamatsu R1635 PMT running at -1000 V. The BaF_2 was coupled to the H6610MOD (also at +1750 V) because the silica window that PMT possesses allows the wavelength the BaF_2 emits. The BaF_2/BaF_2 experiment used no timing probe but was a test to see the lowest time resolution possible; this test showed the need for an equipment upgrade.

The Canberra 454 CFD arrived about the same time that the TN-7200 MCA failed and the new Amptek 8000A MCA was purchased. The results with the new CFD showed a great improvement in the results.

Crystal/Detector	Crystal size	Delay (ns)	Threshold (-mV)	FWHM (ns)
LSO	3.9 x 3.9 mm^2 20.0 mm high	1.0	351	0.51
PVT	10.0 mm diameter 18.8 mm high	5	300.3	0.46
BaF_2	12.5 mm diameter 12.7 mm high	2.0	250.0	0.40
BaF_2/BaF_2	12.5 mm diameter 12.7 mm high	2.0	250.0	0.23
$LaBr_3$	16.3 mm diameter 19.9 mm high	1.0	548	0.44
LYSO	13.0 mm diameter 12.9 mm high	1.0	499	0.49
HiRez (13×13)	4.0×4.0×20 mm^3	6	299.9	0.62
HR+ (8×8)	4.05×4.39×30 mm^3	25	125.0	1.6
Focus (12×12)	1.51×1.51×10 mm^3	6	50.0	0.96

Table 4–3: Time resolution results from the new probe using the Canberra 454 CFD. The time resolutions are much improved and the BaF_2 /BaF_2 result of 0.23 ns is in the range that we desired. Each of the individual crystal were coupled to the Hamamatsu H6610MOD PMT. The timing probe and PMTs were operated at +2000 V (for H6610) and -2000 V (for H6610MOD). The timing probe also had a threshold of -200.0 mV and a CFD delay of 3.5 ns for each experiment except for the HR+ test where the timing probe delay was 2 ns. The LSO crystal is square faced (as are the crystals in the three block detectors) but the remaining five scintillators are cylindrical.

The results using the new probe with the Canberra 454 CFD were very good; the higher performing equipment proved to decrease the time resolution significantly. This can be attributed to the improved and adjustable time walk of

the Canberra 454 CFD but also, especially in the case of the HR+ improvement, on the 454's acceptance of a larger array of delays. The delay of the Ortec CF8000 is selected internally and only has five options, the Canberra 454 allows the user to select any delay greater then 0.6 ns with the use of an external cable.

4.2 Energy Spectra from Each Detector from a Sodium-22 Source

First shown are a series of plots from individual crystal/PMT combinations. Figures 4–1 through 4–4 show those results, from which it is clear $LaBr_3$ has the best energy resolution. Next shown is a series of plots taken with the HiRez detector. The performance of the source from the new and old probe is shown. The values for the efficiency demonstrate the value of the stronger source. This is also demonstrated in figure 4–6 where the sodium spectra are barely visible in the presence of the LSO background.

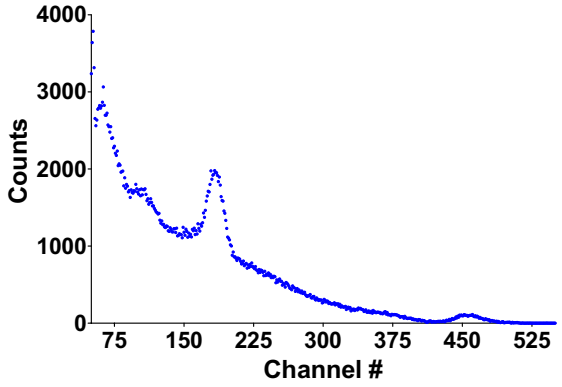

Figure 4–1: ^{22}Na spectrum taken with the 3.9×3.9×20.0 mm^3 LSO crystal. It was coupled to the H6610MOD PMT running at +1300 V. The acquisition was for 2000 s at a distance of 40 cm.

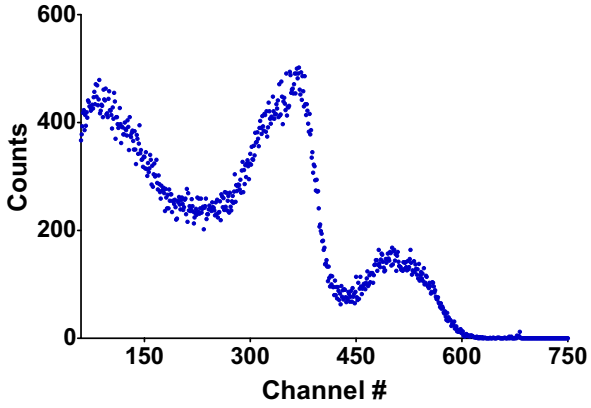

Figure 4–2: ^{22}Na spectrum taken with the 10.0 mm diameter and 18.8 mm high cylindrical PVT detector. It was coupled to the H6610MOD PMT running at +2000 V. The acquisition was for 2000 s at a distance of 40 cm. The small count rate is due to the low detection efficiency of PVT to high energy photons. This lack of efficiency is because of the low density of the plastic.

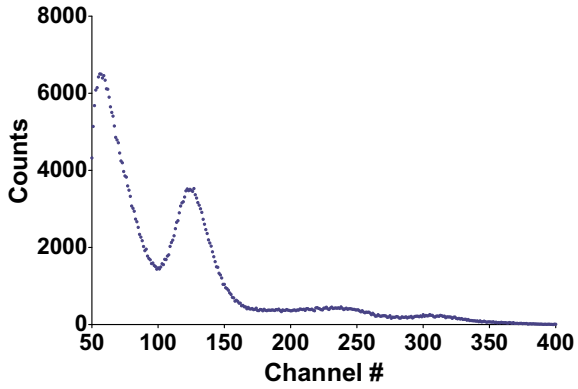

Figure 4–3: ^{22}Na spectrum taken with the 12.5 mm diameter and 12.7 mm high cylindrical BaF_2 detector. It was coupled to the H6610MOD PMT running at +2000 V. The acquisition was for 2000 s at a distance of 40 cm.

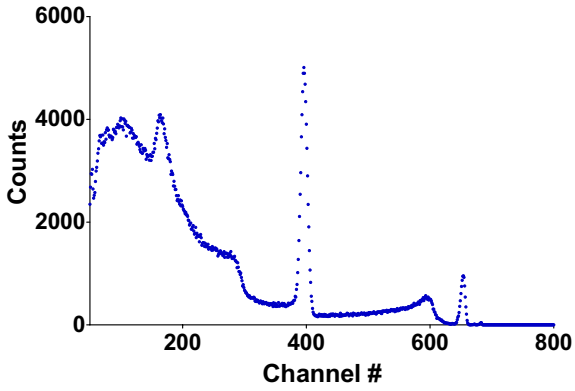

Figure 4–4: ^{22}Na spectrum taken with the 16.3 mm diameter and 19.9 mm high cylindrical $LaBr_3$ detector. Note that there is a casing around this crystal (included in the size) because $LaBr_3$ is hygroscopic. It was coupled to the H6610MOD PMT running at +1300 V. The acquisition was for 2000 s at a distance of 40 cm. The very good resolution of $LaBr_3$ is attributed to its high light output.

The HiRez detector energy spectrum was experimented from several distances and with both the old and new probe. At the time of these experiments the activity of the new probe was 21 times that of the old probe. The extra measurements were done to reflect the real results that would be seen in a true scanner and to see the effect of the background radiation from the LSO.

Figures 4–7 and 4–8 represent the same data as figures 4–5 and 4–6 but the background from the LSO has been subtracted from the signals, leaving just the ^{22}Na spectra. The figure 4–9 is from the same experiment again, but all the HiRez spectra plotted with the all results from the old probe multiplied by 21, the difference in activities at the time of the experiment.

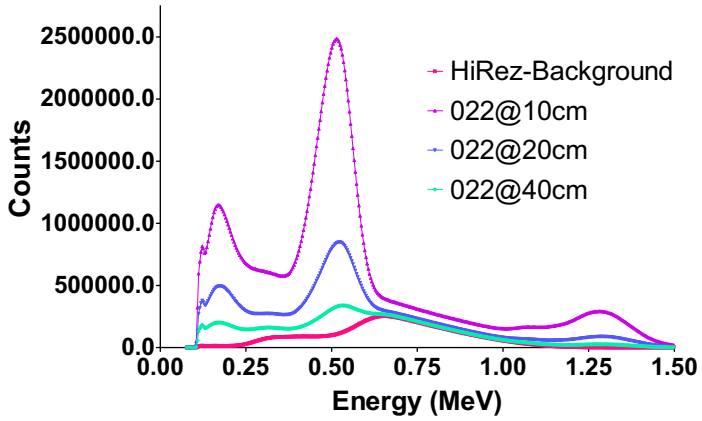

Figure 4–5: A series of ^{22}Na spectra and one spectrum (pink) that is the background radiation taken with the HiRez detector, primarily due to the radioactive LSO. Clearly, as the source is moved close to the detector the sodium spectrum is seen more easily above the LSO spectrum. The efficiency of the detector in the 350 keV to 650 keV window is 89% when the source is 10 cm away, 73% when 20 cm away and 46% at 40 cm away. The voltage of the HiRez detector was dropped to 890 V because the amplifier was saturated at higher voltages and the data was taken for 2000 s in each case. This data was taken using the Amptek 8000A MCA. Note: 022 is the serial number of the new probe.

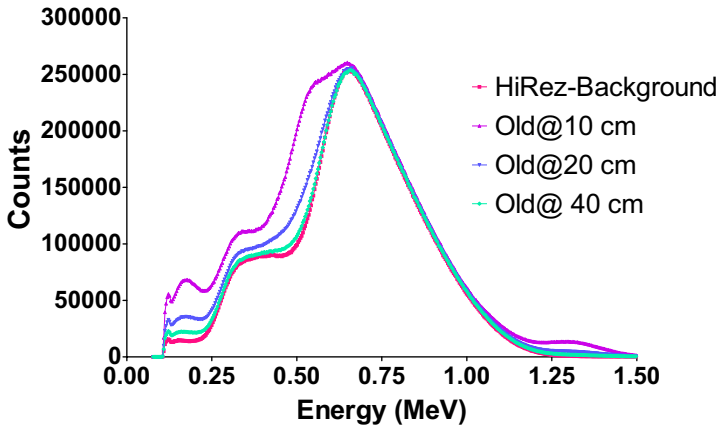

Figure 4–6: The same experiment as above but using the old probe, which at the time of the experiment, had 21 times less activity. It is much harder to see the sodium spectrum above the background from the LSO. The efficiency in a 350 keV to 650 keV window is 28% at 10 cm, 11% at 20 cm and only 3% at 40 cm. The voltage of the HiRez was also 890 V and the experiments were 2000 s and also used the Amptek 8000A MCA.

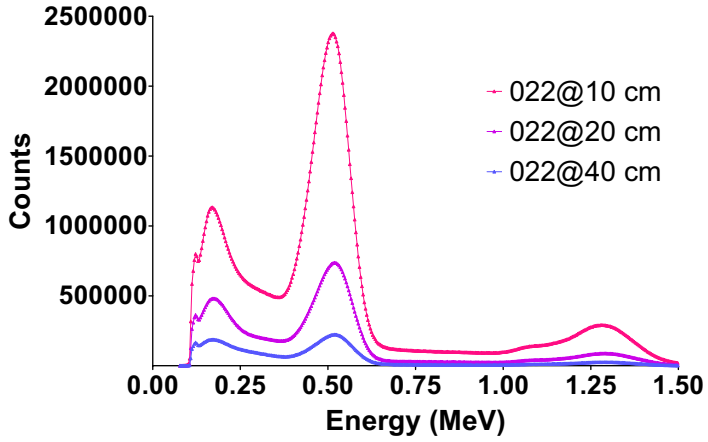

Figure 4–7: The ^{22}Na spectra from the new probe with the HiRez LSO background subtracted.

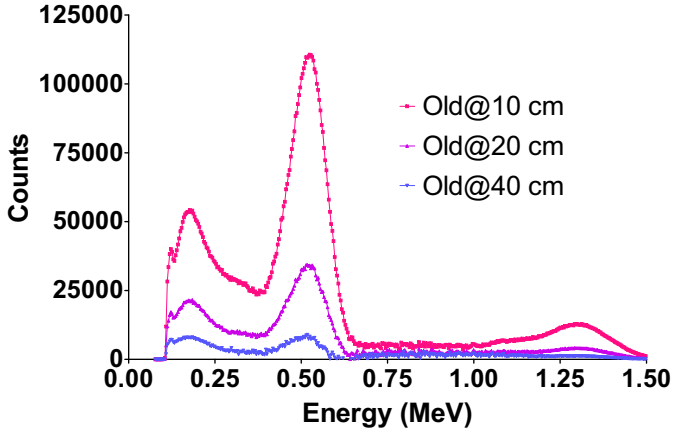

Figure 4–8: The ^{22}Na spectra from the old probe with the HiRez LSO background subtracted.

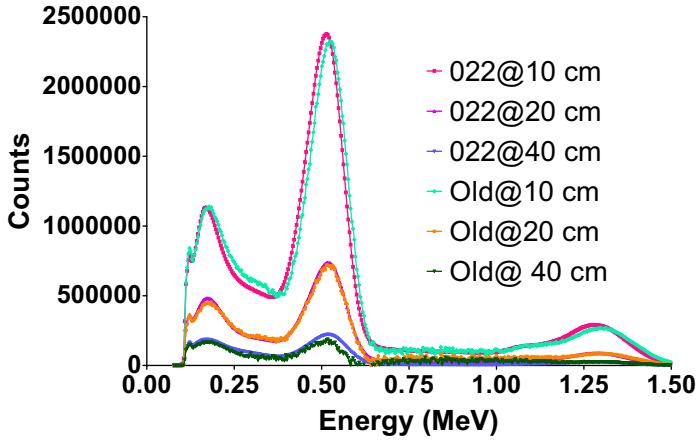

Figure 4–9: All HiRez spectra with the LSO subtracted and the old probe spectra multiplied by 21, the difference in activity at the time of the experiment. All data that is done from the same distance looks similar, showing there are no dead time problems and that the data scales properly from the hot source to the cold one.

Figure 4–10 shows the ^{22}Na energy spectrum taken with the HR+ detector. Since there is no background radioactivity, there is no need for the analysis that was previously done on the HiRez detector.

Figure 4–11 and 4–12 show the ^{22}Na spectrum taken with a Focus detector, with and without the LSO background, respectively. The large amount of Compton data is due to the much smaller crystal size on the Focus detector as compared to the HiRez detector.

4.3 Crystal to Crystal Time Differences in the HiRez and Focus Detectors

Using the setup shown in section 3.2.3 the time and energy spectra can be examined from each individual crystal in the block. These tests were done

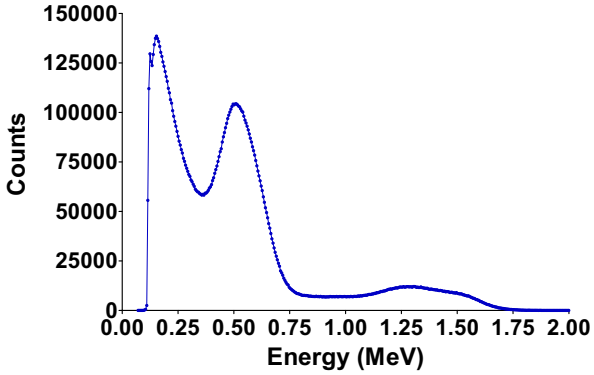

Figure 4–10: ^{22}Na spectrum with the HR+ block detector. The supplied voltage was +1300 V and the acquisition time was 2000 s. This experiment used the Amptek 8000A MCA.

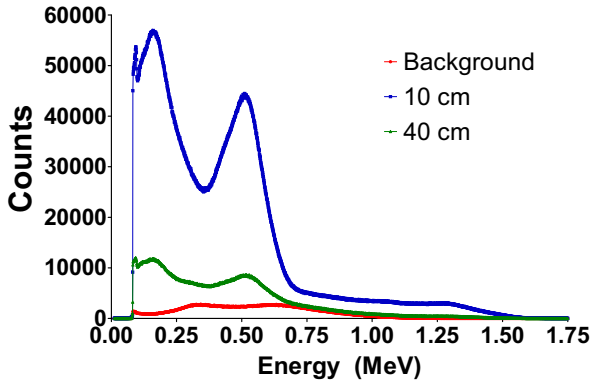

Figure 4–11: The ^{22}Na spectrum taken with the Focus detector as well as the background spectrum. The voltage on the detector was 715 V and the acquisition time was 2000 s. The large amount of data in the Compton region is due to the small crystals limiting the number of multiple interactions in the crystal.

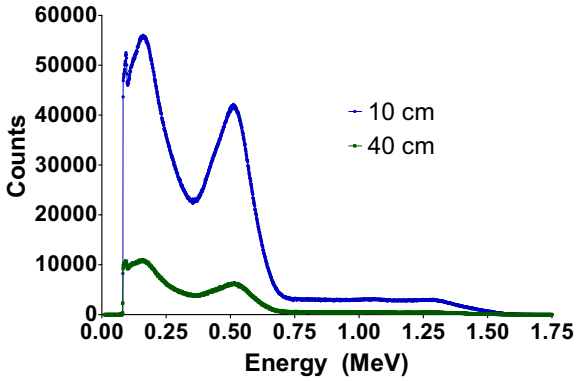

Figure 4–12: The ^{22}Na spectrum taken with the Focus detector with the LSO background subtracted. The efficiency at 10 cm is 92% and at 40 cm is 64% (350 keV to 650 keV window).

on the two high performing detectors that we had: the Siemens HiRez and Focus detectors. Both detectors use LSO as the scintillator which is the most commonly used crystal in detectors requiring good time resolution. The focus of this section is on the time of flight errors that would be encountered on a crystal by crystal basis due to timing differences. As well, any improvement seen in the time resolution can also be employed to randoms reduction. Also shown will be the differences in the positions of the energy peaks in the same block, but different crystals and the improvement that can be made in the energy spectrum if this is considered. Unfortunately, due to equipment limitations in this setup, the detectors could not be completely optimized for time resolution. The amplifier we used would saturate before the detectors would reach its maximum running voltage, so the blocks did not have the lowest time resolution that was

found. Even though this is the case, the differences in the crystal to crystal time properties are evident.

4.3.1 The HiRez Detector

First, to demonstrate the effect of time arrival differences, I will show an exaggerated example. Figure 4–13 shows what a normal series of images should look like when the arrival times from each PMT in the detector are about the same. The subsequent three figures have the signal from one PMT slowed or sped up by changing the length of the cable connecting it to the equipment. In figure 4–14 the cable was switched from the normally used 164 cm cable to a longer 218 cm cable, thus making the signal arrive 2.84 ns later then it normally would (based on 19 ns/cm signal speed in the cable). Figure 4–15 has a cable that is 67 cm shorter than normal, making the signals arrive 3.53 ns early and, finally, figure 4–16 uses a cable that is 96 cm shorter than normal, resulting in the signals arriving 5.05 ns early.

When testing the HIRez detector with the new, high performance probe, the timing and energy information was gathered and fit for each crystal. In the case of the energy information, it was rescaled to the peak so that each crystal put the peak in the same channel (and moved other data as well). This greatly improved the energy resolution of the detector. In the case of the time information it was fit on the DEC Alpha open VMS system and plotted by arrival time as well as its resolution. Figure 4–17 shows the energy spectrum from four crystals that are situated above the four PMTs and the sum of those signals. It is clear, just from this small sample, that each crystal does not exhibit the same characteristics.

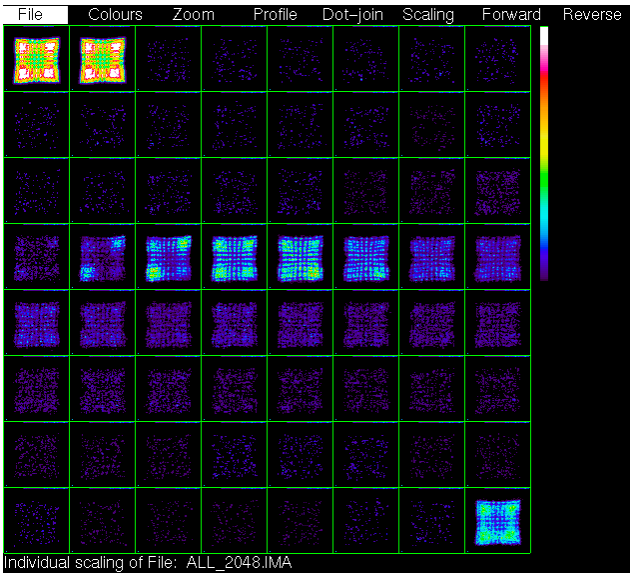

Figure 4–13: Images (binned by time) when all PMT's have their data arrive at nearly the same time.

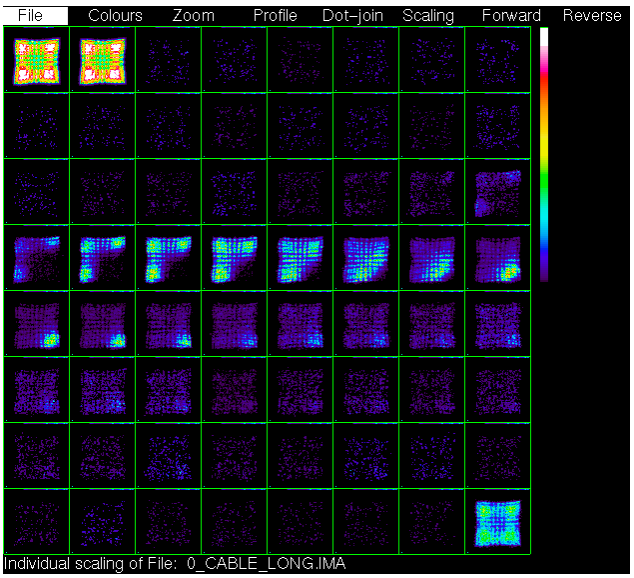

Figure 4–14: Bottom right PMT signals arriving 2.84 ns late

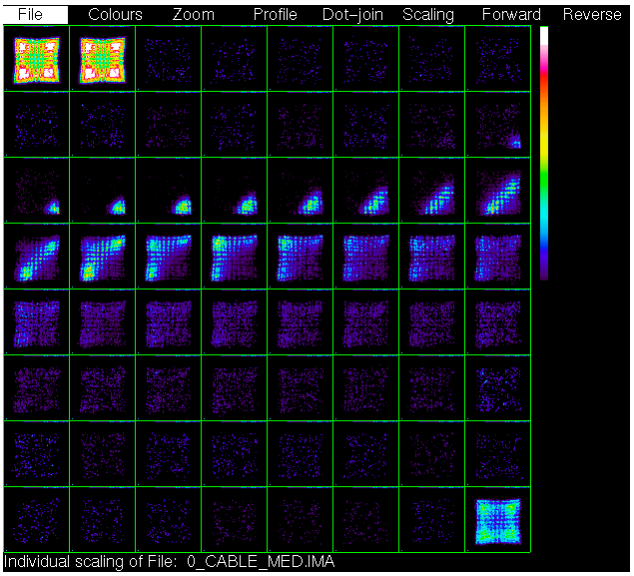

Figure 4–15: Bottom right PMT signals arriving 3.53 ns early

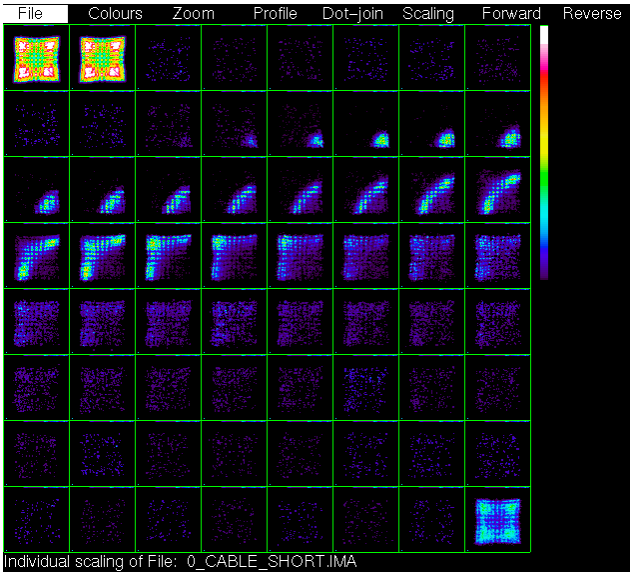

Figure 4–16: Bottom right PMT signals arriving 5.05 ns early

Figure 4–18 shows the sum of four crystals over the PMTs as well as the sum of the four corner crystals as well as the energy spectrum for the entire block (divided by 50). Again it is clear that without any realignment, the total energy resolution of the block is degraded. Figure 4–19 shows the unmodified energy data as well as the rescaled data. The improvement when the rescaling occurs is clear.

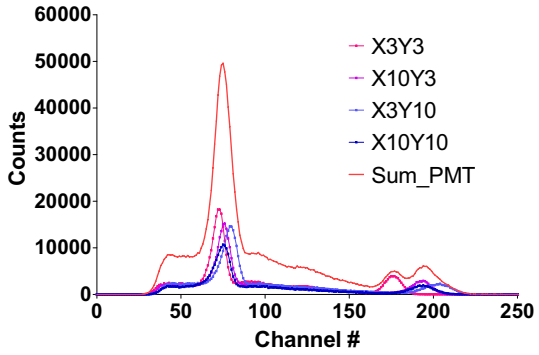

Figure 4–17: The energy spectrum from four crystals in the HiRez detector, one over each PMT. Also shown is the sum of those signals. It is clear that they do not all peak at the same channel.

Figure 4–20 shows the peak channel of each crystal in the block. The higher the bar the higher the peak channel. The resolution of each crystal is shown in figure 4–21. The resolution of the entire block for that experiment was 1.31 ns.

Figure 4–22 has the largest implications in a scanner and especially a time of flight scanner. This plot shows the arrival time differences in each crystal (in coincidence with the positron emission). Differences in bar height/colour shown

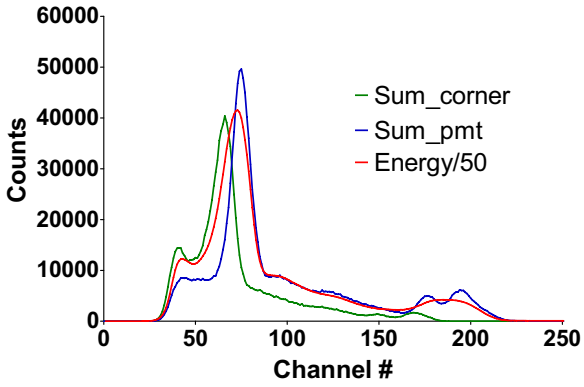

Figure 4–18: The sum of all four corner crystals as well as the four PMT crystals. Also shown is the energy spectrum for the entire block (divided by 50). Again, it is clear that not all peaks are in the same channel.

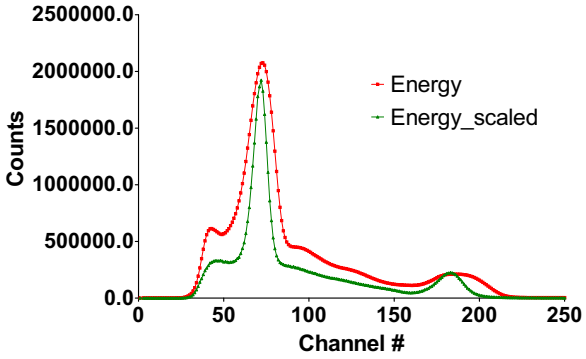

Figure 4–19: The raw HiRez Energy spectrum (red) and the rescaled spectrum (green). There is definite improvement seen in the 511 keV peak, but a very substantial improvement in the 1.2745 MeV peak. The scaled spectrum includes fewer counts because the crystal selection process does not include some of the data in the entire block.

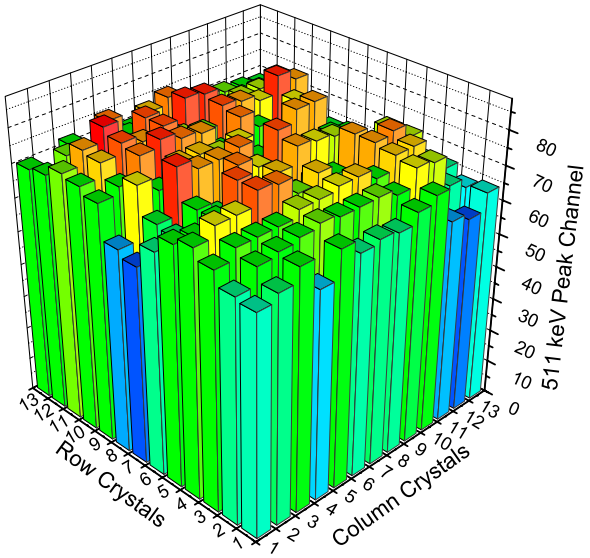

Figure 4–20: The channel of the 511 keV peak in the HiRez block. The max channel is 82 and the min is 57. The average channel position is 72.1 with a standard deviation of 5.5. The red bars are the higher peak channels and the blue are the lower channels.

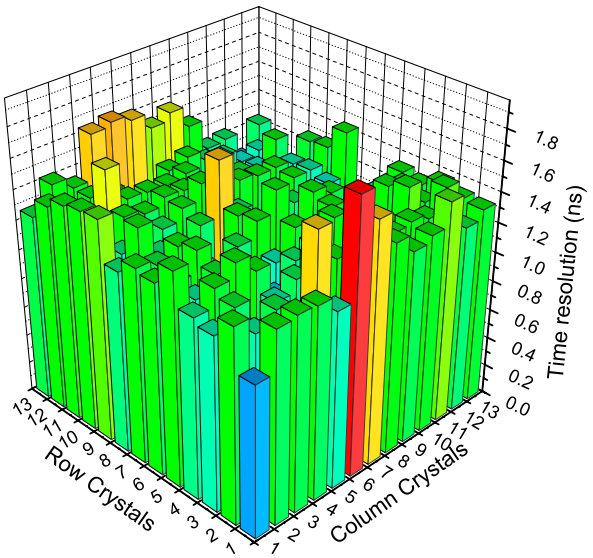

Figure 4–21: The time resolution for each crystal in the HiRez detector. As with the previous plot, the higher/more red bar indicated a larger (worse) time resolution. The maximum resolution is 1.827 ns and the lowest is 0.862 ns. The average is 1.26 ns with a standard deviation of 0.16 ns.

in this plot will result in systematic time of flight differences in the data. If two crystals that were in coincidence with each other in a scanner had these differences, every annihilation detected by them would be misplaced. The best possible plot would have a flat top and be a single colour. The largest difference seen in this one detector is 0.53 ns, which, if these were crystals in coincidence, would result in an annihilation misplacement of about 8 cm. An 8 cm misplacement is unacceptable. Notice that two of the corners arrive much later then the other two corners. This could be explained by the gain of all four PMTs not being optimized for the voltage the detector was operated against. Since the gain adjust simply changes the voltage on one of the dynodes, this could affect each PMT differently.

The consequence of each of these experiments shows that any accuracy in either time or energy would benefit from using a crystal by crystal setting rather then one setting for an entire block. In the energy domain the window used could be made much narrower if there is one window used for each crystal. This would result in an overall reduction in scatter due to a narrower energy window being used, which is why most modern scanners employ this method. In the time domain the alignment should be done for each crystal rather then each block. There would be a reduction in random counts due to a narrower timing windows being used. A larger consequence is in time of flight scanners where figure 4–22 shows that performing an alignment on a crystal by crystal basis should be required. Figure 2–8 shows the consequences of a 1 ns misalignment of 2 crystals.

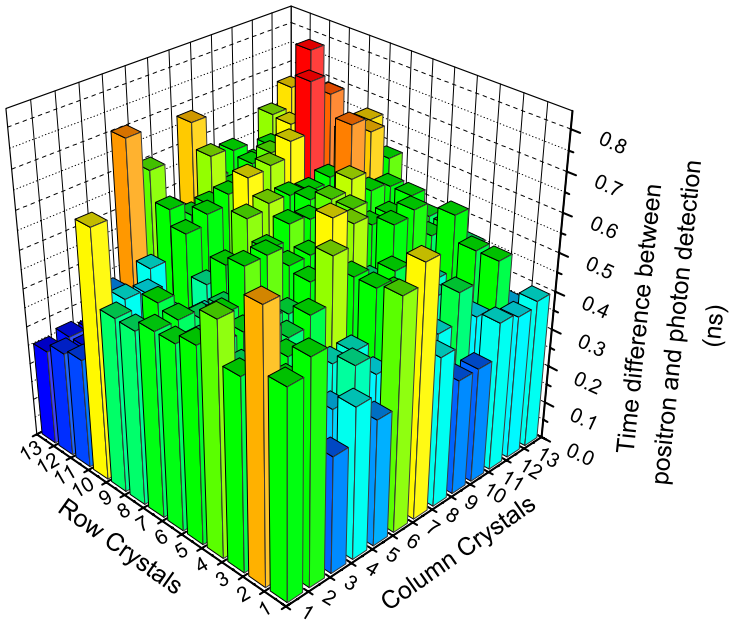

Figure 4–22: The amount of time after the detection of a positron by the timing probe that the photon is detected by the HiRez detector. For an ideally time aligned detector this plot would be flat. Differences here will lead to time of flight differences that should not exist. The imperfection will also lead to a worse time resolution. The minimum time of arrival is 0.252 ns and the max is 0.781 ns. The average time is 0.495 ns with a standard deviation of 0.114 ns.

4.3.2 The Focus Detector

The focus detector is made of the same crystal, LSO, as the HiRez detector, but the crystals are smaller and the PMTs that are used are position sensitive. The increased spatial resolution from the PMTs is immediately obvious when an image is seen (figure 4–23). As it will be seen, there is a trade-off in time accuracy in order to gain this spatial information.

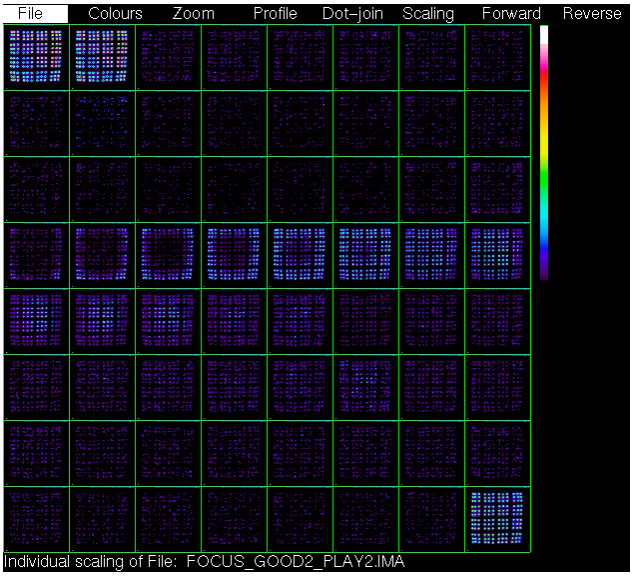

Figure 4–23: Sample of images from the focus detector, note the very high spatial resolution. Even without any analysis, inconsistent time characteristics can be seen. The information from the outer crystals arrive before that of the inner crystals (this is seen more clearly in figure 4–29).

Analogous to the figures shown in section 4.3.1 shown in figure 4–24 is the signal from four crystals which are over the PMT, figure 4–25 is the sum of the signals from four crystals over the PMT and the four corner crystals as well as the energy signal from the entire block (divided by 46 in order to be in the same

scale). Finally, figure 4–26 shows the improvement in the energy spectrum when the data is rescaled so all the crystals have the 511 keV peak at the same channel. It is clear from the four PMT crystals that a very different energy spectrum is coming from each of the crystals and the blurred peak of the sum shows this consequence. The sum of the PMT crystals and the sum of the corner crystals also demonstrates this same problem across the entire block. Figure 4–25 shows the improvement that can be had by rescaling the data. Not only is the improvement in the 511 keV very impressive, the 1.2745 MeV peak is quite prominent when rescaled whereas it could not even be seen in the raw data. Clearly, the advantage of the rescaling can be seen and justifies why this is used in modern scanners.

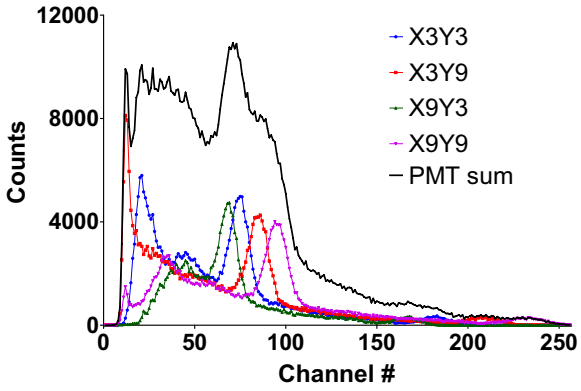

Figure 4–24: Signals from four crystals which are above the PMTs in the Focus detector. The spread just amongst these is clear.

Figure 4–27 shows the peaks of the crystals on a bar graph. The redder and taller a bar, the larger the channel the 511 keV peak is in. There is more variation in this detector than in the HiRez detector. This leads to the even more significant

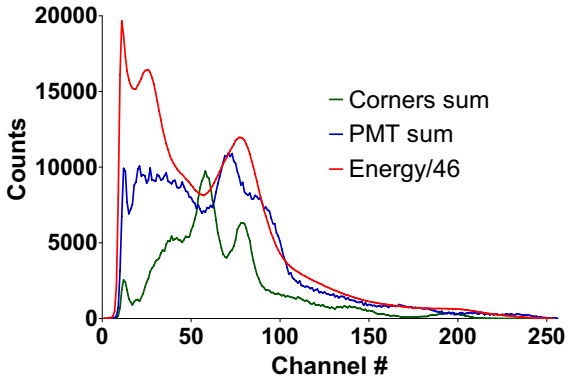

Figure 4–25: Shown is the sum of the same four crystals above the PMTs, as well as the four corner crystals and the energy spectrum for the entire Focus detector (divided by 46 for scale).

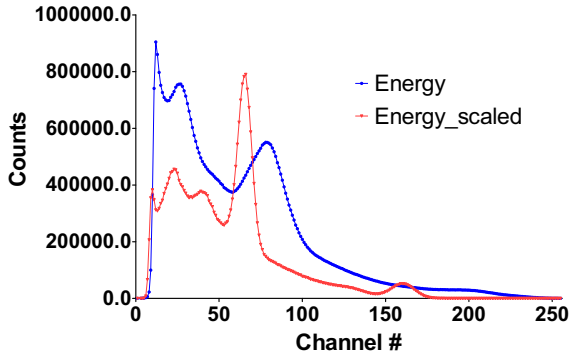

Figure 4–26: The energy spectrum for the raw Focus data and for the rescaled focus data. Clearly the energy resolution is improved greatly at both the 511 keV peak and the 1.2745 MeV peak.

improvement in the energy spectrum from the data scaling. The average channel is 78.4 with a standard deviation of 9.0 and a maximum and minimum of 96 and 57, respectively. There also seems to be some systematic difference from the low column crystals to the high column crystals.

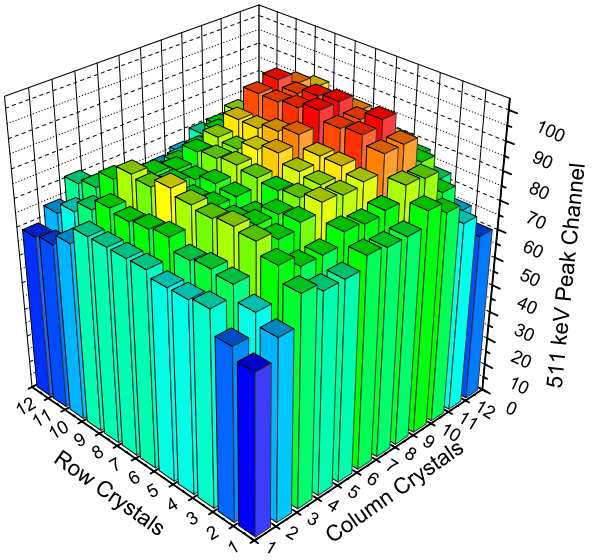

Figure 4–27: The 511 keV peak positions in the Focus detector. The variation here is greater than in the HiRez detector leading to larger improvement when the data is rescaled.

Figure 4–28 shows the time resolution (in ns) for each crystal in the Focus detector. This data seems to be comparable to the HiRez detector, but there does seem to be some systematic effects in the Focus detector. As show in figure 4–29 there is circular symmetry in the arrival time and there may be some circular

effect in the resolution as well. The average resolution in the Focus block is 1.21 ns with a standard deviation of 0.170 ns. The max and min are 1.532 and 0.823.

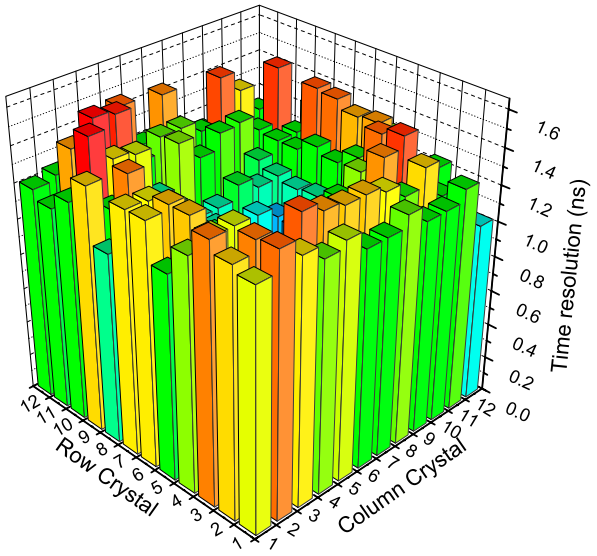

Figure 4–28: The time resolution for each crystal in the Focus detector.

The most striking plot, not just because of the large time differences, but also because of the systematic errors, is the bar graph of the difference between the positron detection (from the timing probe) and the photon detection in the focus detector. Clearly the outer crystals detect the photons earlier than the inner crystals. This effect may be caused by the operation of the position sensitive PMT. There is a resistor chain through the anodes of the PS-PMTs and this may cause the signal to be slowed, which would result in the patterns seen in figure 4–29. Not only is this very systematic, but it is also very large. The maximum difference is

1.648 ns and the minimum is 0.281 ns. This difference would result in a time of flight error of 20.5 cm, about half the diameter of a human whole body scanner bore. The average time is 1.02 ns with a standard deviation of 0.39 ns.

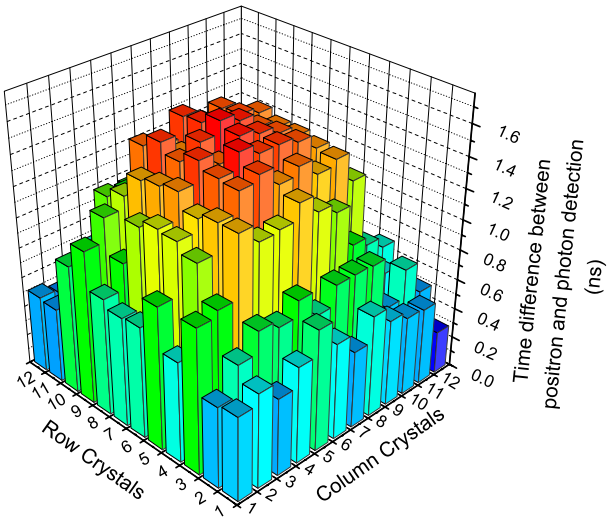

Figure 4–29: Difference in positron and photon detection in the Focus detector. Clearly there is a significant and systematic error here, likely caused by the use of a position sensitive PMT.

CHAPTER 5
Conclusion and Future Work

We have shown the need for crystal by crystal timing alignment and that it would prove beneficial in a PET scanner. Especially demanding, from a time perspective, are time of flight PET scanners. These scanners use the difference in arrival times of two photons from an electron-positron annihilation event to place the position of the event. Since light travels 30 cm in 1 ns, precision in measuring this time difference is essential. Currently Philips Medical has the only commercially available time of flight scanner. It has a reported time resolution of 650 ps. Using the Siemens HiRez and Focus detectors as examples, we saw the large variation in the time stamp recorded by each crystal that would have a significant impact on the quality of time of flight scanners. In conventional scanners improving the time alignment would also improve image quality by reducing the number of random counts.

The energy spectrum for each crystal also showed significant variance that should be taken into account. To demonstrate the improvement that can be made, the data was rescaled to have the 511 keV peak in the same channel for each crystal; the result was a vastly improved energy resolution.

The timing calibration probe that has been developed facilitates an improved method for time alignment. The primary improvement in the calibration comes from the time required to perform it. Since this method is not iterative, and

does not require two detected annihilation photons in coincidence. Instead, it requires a detected positron emission and one annihilation photon, and a simple photon time arrival plot. The lack of iterative methods reduces the time by not simply guessing what may improve the time alignment, but instead having a common time reference, the positron emission. Each detector's offset is aligned to the positron emission. Needing just the one photon to be detected increases the efficiency in two ways: one simply because the probability of detecting one photon is greater then that of two photons and the second because, if both photons are detected, then a count is applied to the alignment of two detectors.

The alignment of PET scanners can be improved with the alignment probe for two reasons. The decreased time required to perform the calibration means that the alignment can be done more often,, facilitating a better long term alignment. The other reason is simply that a more accurate alignment can be done because of the time accuracy improvement over that of the iterative method.

Future work includes a redesign of the ^{22}Na/scintillation combination. It was found that the efficiency of the timing probe was much lower than we had hoped (in Appendix I). Also, for commercial applications, the H6610 PMT is not required, the less costly H6533 may be used. The only difference between the two PMTs is the material the window is made of. The H6610 was chosen so BaF_2 could be coupled to it for testing. Results from other detectors as well as testing on an entire scanner should also be done.

CHAPTER 6
Appendix I: The Timing Probe

Figure 6–1 shows the process to select the appropriate threshold for the timing probe. The chosen threshold was -200 mV at -2000 V, this was in a region that showed stability and also had a good time resolution. The results were with the timing probe in coincidence with a BaF_2 crystal.

The count rate and efficiency of the probe are shown in figures 6–2 and 6–3. At the time of the experiment the activity of the source was 3.414 MBq (92.2 μCi). The efficiency at the parameters used was about 3%. This is much lower then desired and will hopefully be improved in the future.

The schematic drawing of the probe is shown in figure 6–4. The exposed end of the PMT is capped with a broom hanger. The PMT is light sealed in the carbon fiber pipe with black electrical tape.

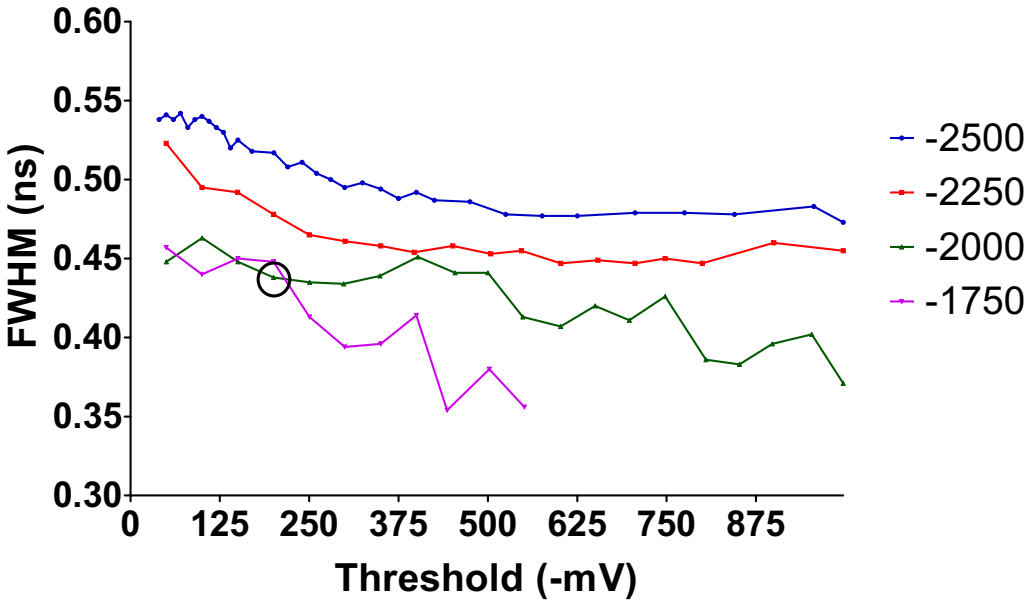

Figure 6–1: Threshold selection for the timing probe.

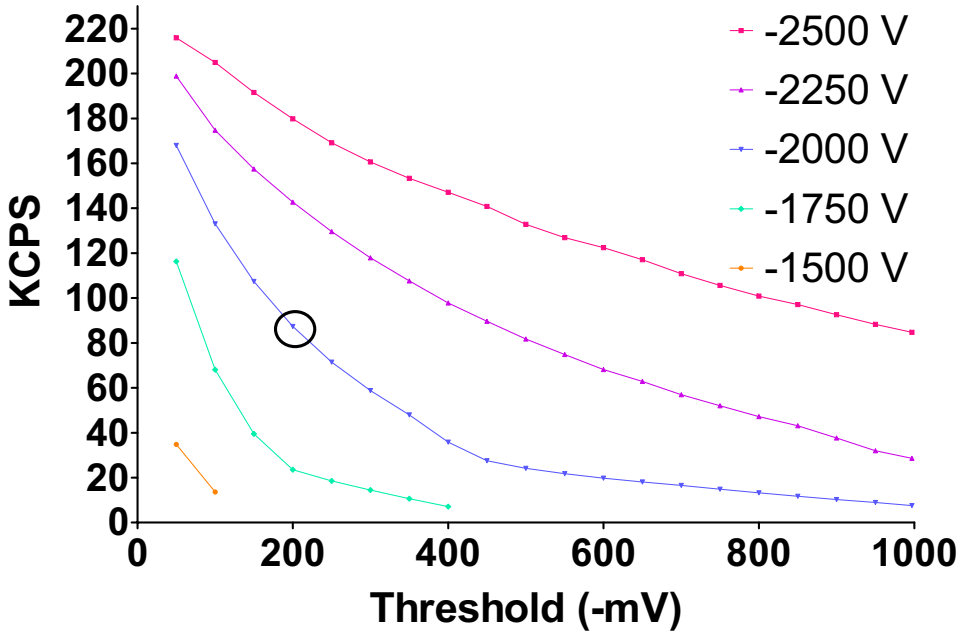

Figure 6–2: The count rate of the timing probe (through a counter, terminated in 50 Ω).

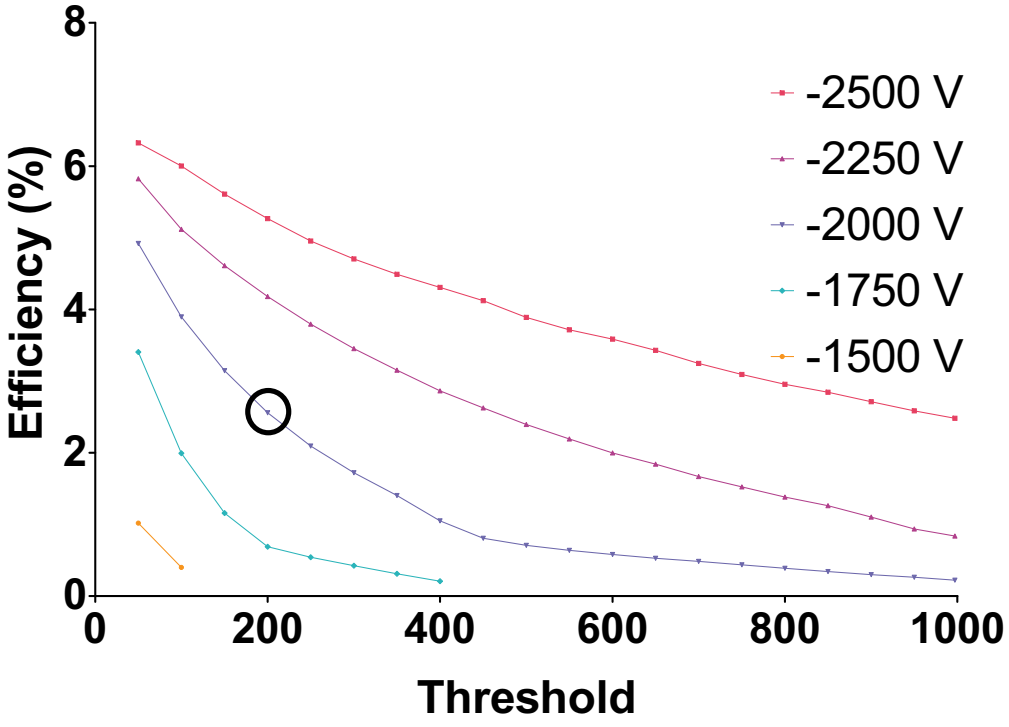

Figure 6–3: The efficiency of the timing probe, at the time of the experiment the activity of the source was 3.414 MBq/92.2 μCi.

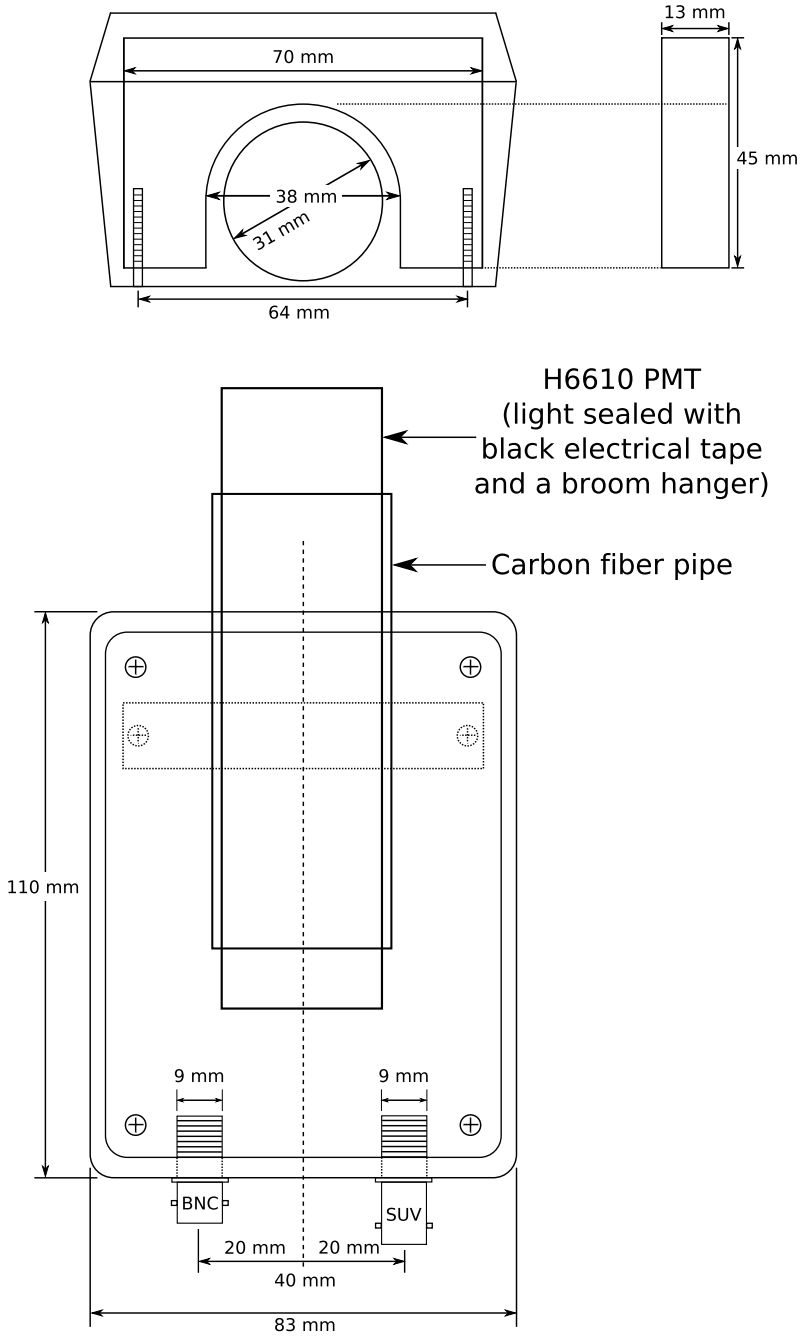

Figure 6–4: Dimensions of the timing probe enclosure.

REFERENCES

[1] P.A.M. Dirac. The quantum theory of the electron. *Proc. R. Soc. London.*, A 117:610–624, 1928.

[2] Interviewed by Harriot Lyle. Carl anderson. Oral History Project, California Institute of Technology Archives., 15 October 2004. Retrieved 5 October 2006 from the World Wide Web: `http://resolver.caltech.edu/CaltechOH:OH_Anderson_C`.

[3] Carl D. Anderson. The positive electron. *Phys. Rev.*, 43:491, 1933.

[4] S.J. Tao. Positron annihilation in molecular substances. *J. Chem. Phys.*, 56(11):5499–5510, 1998.

[5] G. Tarnopolaky et al. Hadron production by electron-positron annihilation at 5 GeV center-of-mass energy. *Phys. Rev. Lett.*, 32(8):432–435, 1998.

[6] Gopal Saha. *Basics of PET Imaging*. Springer, 2005.

[7] E.B. Podgorsak. *Radiation Physics for Medical Physicists*. Springer, 2005.

[8] Harold E. Johns and John R. Cunningham. *The Physics of Radiology*. Thomas Books, fourth edition, 1983.

[9] Simon R. Cherry, James A. Sorenson, and Michael E. Phelps. *Physics in Nuclear Medicine*. Saunders, third edition, 2003.

[10] Diane C. Chugani et al. Human brain serotonin synthesis capacity measured in vivo with α-[C-11]Methly-L-Tryptophan. *Synapse*, 28:33–43, 1998.

[11] Heinrich R. Schelbert et al. Regional myocardial blood flow, metabolism and function assessed noninvasively with positron emission tomography. *Am. J. Cardiol.*, 46:1269–1277, 1980.

[12] Kazuo Kubota et al. Lung tumot imaging by positron emission tomography using C-11 L-Methionine. *J. Nucl. Med.*, 26:37–42, 1985.

[13] Kiyoshi Murata et al. Ventilation imaging with positron emission tomography and nitrogen 13. *Radiology*, 158:303–307, 1986.

[14] Nobusada Shinoura et al. Brain tumors: Detection with C-11 PET. *Radiology*, 202:497–503, 1997.

[15] Robert E. Reiman et al. Imaging of brain tumors after administration of L-(N-13)Glutimate: Concise communication. *J Nucl. Med.*, 23:682–687, 1982.

[16] Timothy J McCarthy and Michael J. Welsh. The state of positron emitting radionuclide production in 1997. *Semin. Nucl. Med.*, 28(3):235–246, 1998.

[17] Timothy J. Tewson and Kenneth A Krohn. PET radiopharmaceuticals: State-of-the-art and future prospects. *Semin. Nucl. Med.*, 28(3):221–234, 1998.

[18] R. Nickles. Production of a broader palette of PET tracers. *J. Label. Compd. Radiopharm.*, 46:1–27, 2003.

[19] Wolfram Eckhardt and Johann Hausladen. Radionuclide generator. U.S. Patent 4,239,970, December 1980.

[20] F.F. Knapp Jr. and S. Mirzadeh. The continuing important role of radionuclide generator systems for nuclear medicine. *Eur. J. Nucl. Med.*, 21:1151–1165, 1994.

[21] William Hendee and E. Russell Ritenour. *Medical Imaging Physics*. Wiley-Liss, fourth edition, 2002.

[22] Pat Zanzonico. Positron emission tomography: A review of the basic principles, scanner design and performance, and current systems. *Semin. Nucl. Med.*, 34(2):87–111, 2004.

[23] Ervin Podgorsak, editor. *Radiation Oncology Physics : a handbook for teachers and students*. IAEA, 2005.

[24] S.C. Strother et al. Measuring PET scanner sensitivity: relating count rates to image signal-to-noise ratios using noise equivalents counts. *IEEE Trans. Nucl. Sci.*, 37(2):783–788, 1990.

[25] Charles Stearns et al. NECR analysis of 3D brain PET scanner designs. *IEEE Trans. Nucl. Sci.*, 42(4):1075–1079, 1995.

[26] W. W. Moses. Advantages of improved timing accuracy in PET cameras using LSO scintillator. *IEEE NSS Conference Record*, 3:1670– 1675, 2002.

[27] Glenn F. Knoll. *Radiation Protection and Measurement*. Wiley, third edition, 1999.

[28] Bernard Salzberg. Phototube. U.S. Patent 1,980,702, November 1934.

[29] Philippe Bourgeois et al. Performance of the photomultiplier tubes used in the DIRC of BABAR: effect of a magnetic field and of helium. *Nucl. Instrum. Meth A*, 442:105–112, 2000.

[30] Yiping Shao et al. Simultaneous PET and MR imaging. *Phys. Med. Biol.*, 42:1965–1970, 1997.

[31] C.L. Melcher and J.S. Schweitzer. Scintillation properties of GSO. *IEEE Trans. Nucl. Sci.*, 37(2):161–164, 1990.

[32] Catherine Michelle Pepin et al. Properties of LYSO and recent LSO scintillators for phoswich PET detectors. *IEEE Trans. Nucl. Sci.*, 51(3):789–795, 2004.

[33] W. Mengesha et al. $Gd_2SiO_5(Ce^{3+})$ and BaF_2 measured electron and photon responses. *Nucl. Instrum. Meth. A*, 486:448–452, 2002.

[34] Saint-Gobain Crystals. Scintillation products. Product Manuals. `http://www.detectors.saint-gobain.com/data/aboutus/about_Us.asp?seq=700&Lang=US`.

[35] Charles Melcher. Scintillation crystals for PET. *J. Nucl. Med.*, 41:1051–1055, 2000.

[36] E. Loef et al. High-energy resolution scintillator: Ce^{3+} activated $LaBr_3$. *Appl. Phys. Lett.*, 79(10):1573–1575, 2001.

[37] T. Kimble et al. Scintillation properties of LYSO crystals. *IEEE NSS Conference Record*, 3:1434–1437, 2002.

[38] Burle Industries Inc. *Photomultiplier Handbook*. Burle Technologies Inc., 1980.

[39] Robert Pringle. The scintillation counter. *Nature*, 166:11–14, 1950.

[40] Hal Anger. Scintillation camera with multichannel collimators. *J. Nucl. Med.*, 5:515–531, 1964.

[41] Bernd J. Pichler et al. Performance test of an LSO-APD detector in a 7-T MRI scanner for simultaneous PET/MRI. *J. Nucl. Med.*, 47:639–647, 2006.

[42] Hamamatsu Photonics K.K. Characteristics and use of Si-APD (avalanche photodiode). Product Manuals. `http://sales.hamamatsu.com/assets/applications/SSD/Characteristics_and_use_of_SI_APD.pdf`.

[43] K. Kuroda S. Yamamoto and M. Senda. Scintillator selection for MR-compatible gamma detectors. *IEEE Trans. Nucl. Sci.*, 50(5):1683–1685, 2003.

[44] Margaret E. Daube-Witherspoon et al. Post-injection transmission attenuation measurements for PET. *IEEE Trans. Nucl. Sci.*, 35(1):757–761, 1988.

[45] Wencke Lehnert et al. Evaluation of transmission methodology for the microPET Focus 220 animal scanner. *IEEE NSS Conference Record*, pages 2519–2523, 2005.

[46] Eddie Xu et al. A segmented attenuation correction for PET. *J. Nucl. Med.*, 32:161–165, 1991.

[47] A. J. Becher et al. Methods to reconstruct emission and transmission data in 3D PET. *IEEE Nuclear Science Symposium*, 2:1082–1086, 1997.

[48] T. K. Moon. The expectation maximization algorithm. *IEEE Signal Processing Magazine*, 13(6):47–60, 1996.

[49] W. W. Moses and M. Ullisch. Factors influencing timing resolution in a commercial LSO PET camera. *IEEE Trans. Nucl. Sci.*, 53(1):78–85, 2006.

[50] Charles W. Stearns. Sorter for coincidence timing calibration in a PET scanner. U.S. Patent 5,272,343, December 1993.

[51] John J. Williams. Automated coincidence timing calibration for a PET scanner. U.S. Patent 5,272,344, December 1993.

[52] John J. Williams et al. Method and apparatus for timing calibration in a PET scanner. U.S. Patent 7,129,495 B2, October 2006.

[53] Mark Lenox et al. Coincidence time alignment of high resolution planar detectors. *IEEE NSS Conference Record*, 2:956–959, 2002.

[54] C.L. Melcher and J.S. Schweitzer. Scintillation properties of GSO. *IEEE Trans. Nucl. Sci.*, 39(4):502–505, 1992.

[55] R.J. Gehrke et al. Half-life of ^{176}Lu. *Phys. Rev. C*, 41(6):2878–2882, 1990.

[56] C. J. Thompson and M-L Camborde. An instrument to facilitate and improve the timing alignment of a PET scanner. U.S. Patent 7,247,844 B2, July 2007.

[57] C. J. Thompson et al. A central positron source to perform the timing alignment of detectors in a PET scanner. *IEEE Trans. Nucl. Sci.*, 52(5):1300–1304, 2005.

[58] D. P. McElroy et al. Use of a central positron emitting reference source to improve the timing alignment of a singles list-mode small animal PET scanner. *IEEE NSS Conference Record*, pages 1620–1623, 2005.

[59] W. W. Moses and C. J. Thompson. Timing calibration in PET using a time alignment probe. *IEEE Trans. Nucl. Sci.*, 53(5):2660–2665, 2006.

[60] Canberra Industries Inc. Model 454 quad cf discriminator user's manual. User's manual, 2000.

[61] Alejandro Levy and Donald Warner. Preventive maintenance system for the photomultiplier detector blocks of PET scanners. U.S. Patent 5,384,699, Jan 1995.

[62] C. J. Thompson and Andrew Goertzen. Measurements on the timing stability of the MicroPET R4 animal PET scanner. *IEEE NSS Conference Record*, 5:2885–2889, 2004.

[63] Hans Reist et al. Study on the stability of the calibration and normalization in PET and the influence of drifts on the accuracy of quantification. *Eur. J. Nucl. Med.*, 15:732–735, 1989.

[64] B. Bengtson and M. Moszyński. Energy-transfer and light-collection characteristics for different types of plastic scintillators. *Nucl. Instrum. Meth.*, 117:227–232, 1974.

[65] Sibylle Ziegler et al. Effects of scintillation light collection on the time resolution of a time-of-flight detector for annihilation quanta. *IEEE Trans. Nucl. Sci.*, 37(2):574–579, 1990.

[66] Randal Slates et al. Design of a small animal MR compatible PET scanner. *IEEE NSS Conference Record*, 2:1268–1273, 1998.

[67] The Institute of Electrical and Electronics Engineers Inc. IEEE standard test procedures for photomultipliers for scintillation counting and glossary for scintillation counting field. Standards Procedure, 1972, 2006. ANSI/IEEE Std 398^{TM}-1972(R2006).

[68] M. M. Ter-Pogossian et al. Photon time-of-flight-assisted positron emission tomography. *J. Comput. Assist. Tomo.*, 5(2):227–239, 1981.

[69] Mikia Yamamoto et al. Experimental assessment of the gain achieved by the utilization of time-of-flight information in a positron emission tomograph (Super PETT I). *IEEE T. Med. Imaging*, MI-1(3):187–192, 1982.

[70] Keizo Ishii et al. High resolution time-of-flight positron emission tomography. *Rev. Sci. Instrum.*, 61(12):3755–3762, 1990.

[71] W . W. Moses and S. E. Derenzo. Prospects for time-of-flight PET using LSO scintillator. *IEEE Trans. Nucl. Sci.*, 46(3):474–478, 1999.

[72] A. N. Bice et al. Monte carlo simulation of BaF_2 detectors used in time-of-flight positron emission tomography. *IEEE Trans. Nucl. Sci.*, 37(2):696–701, 1990.

[73] W. W. Moses. Advantages of improved timing accuracy in PET cameras using LSO scintillator. *IEEE NSS Conference Record*, 3:1670–1675, 2002.

[74] R. Trebossen et al. A study of the signal to noise ratio using time-of-flight information on a positron emission tomograph. *IEEE Eng. Med. Biol.*, 5:1837–1839, 1992.

[75] Thomas Budinger. Time-of-flight positron emission tomography: status relative to conventional PET. *J. Nucl. Med.*, 24:73–78, 1983.

[76] W . W. Moses. Time of flight in PET revisited. *IEEE Trans. Nucl. Sci.*, 50(5):1325–1330, 2003.

[77] Robert Harrison et al. Signal to noise ratio in simulations of time-of-flight positron emission tomography. *IEEE NSS Conference Record*, 7:4080–4083, 2004.

[78] Maurizio Conti. Effect of randoms on signal-to-noise-ratio in TOF PET. *IEEE NSS Conference Record*, 3:1590–1595, 2005.

[79] W. Wang et al. Systematic and distributed time-of-flight list mode PET reconstruction. *IEEE NSS Conference Record*, 3:1718–1722, 2006.

[80] Maurizio Conti et al. First experimental results of time-of-flight reconstruction on and LSO PET scanner. *Phys. Med. Biol.*, 50:4507–4526, 2005.

[81] Joey Kimdon et al. Effect of random and scatter fractions in variance reduction using time-of-flight information. *IEEE NSS Conference Record*, 4:2571–2573, 2003.

[82] Philips Medical Systems. Philips Gemini TF. IEEE Medical Imaging Conference, 2006. `http://www.nss-mic.org/2006/Sponsors/Philips/Philips%20GEMINI%20TF%20PET_CT%20Overview.pdf`.

[83] Ortec. Time-to-amplitude converters and time calibrator. Online Selection Guide. `http://www.ortec-online.com/pdf/tactut.pdf`.

[84] Juha Kostamovaara and Risto Myllylä. A time-to-amplitude converter with constant fraction timing discriminators for short time interval measurements. *Nucl. Instrum. Meth. A*, 239(3):568–578, 1985.

[85] Ortec. 552 linear gate and stretcher. Online manual. `http://www.ortec-online.com/pdf/542.pdf`.

[86] Canberra Industries. Model 2145 time to amplitude converter. User's Manual, 1999.

[87] A. Hallam and R.E. Imhof. Performance tests of a time-to-amplitude converter at high conversion rates. *J. Phys. E: Sci. Instrum.*, 13:520–521, 1980.

[88] Manobu Tanaka et al. Development of monolithic time-to amplitude converter for high precision TOF measurement. *IEEE Trans. Nucl. Sci.*, 38(2):301–305, 1991.

[89] V.P. Ladygin et al. Time-of-flight trigger based on a time-to-amplitude converter. *Instrum. Exp. Tech.*, 44(3):352–358, 2001.

[90] Hoiko Chaborski. Method and apparatus for measuring time. U.S. Patent 4,303,983, Dec 1981.

[91] Jerrold Bushberg et al. *The Essential Physics of Medical Imaging*. Lippincott Williams and Wilkins, second edition, 2002.

[92] Hamamatsu. R1635 photomultiplier tube. Online Specifications Sheet. `http://sales.hamamatsu.com/index.php?id=13189250&language=1&`.

[93] C.C. Lo and B. Leskovar. Evaluation of hamamatsu R1635 photomultiplier. *Rev. Sci. Instrum.*, 55(7):1100–1103, 1984.

[94] Isotope Products Laboratories. `http://www.ipl.isotopeproducts.com/new_ipl_site/`.

[95] R. Sherr and R. H. Miller. Electron capture in the decay of Na^{22}. *Phys. Rev.*, 93(5):1076–1081, 1954.

[96] W. E. Kreger. K capture to positron ratio for Na^{22}. *Phys. Rev.*, 96(6):1554–1555, 1954.

[97] Health Physics Society North Carolina Chapter. Nuclide safety data sheet Sodium-22. `http://www.nchps.org`.

[98] L. Torrisi. Radiation damage in polyvinyltoluene (PVT). *Radiat. Phys. Chem.*, 63:89–92, 2002.

[99] Ortec-ESN. Model cf8000 octal constant fraction discriminator. Operating and Service Manual.

[100] Tracor Northern. TN-7200 multichannel analyzer. Features and Specifications. `http://www.testequipmentdatasheets.com/index_cards/T/Tracor_Northern/TN-7200.pdf`.

[101] Hamamatsu. H6610 photomultiplier tube. Online Specifications Sheet. `http://sales.hamamatsu.com/assets/pdf/parts_H/H6533.pdf`.

[102] Amptek. Multichannel analyzer 'pocket MCA'. User's Manual and Specifications.

[103] Jorway Corporation. Model aurora 14. Specifications Sheet. http://www.jorway.com/pdf/AURORA14.PDF.

[104] GraphPad Prism. http://www.graphpad.com/prism/.

[105] Lars-Eric Adam et al. Performance evaluation of the whole-body PETscanner ECAT EXACT HR$^+$ following the IEC standard. *IEEE Trans. Nucl. Sci.*, 44(3):1172–1179, 1997.

[106] Sara St. James and Christopher Thompson. Image blurring due to light-sharing in PET block detectors. *Med. Phys.*, 33(2):405–410, 2006.

[107] Mehmet Aykac et al. Timing performance of Hi-Rez detector for time-of-flight (TOF) PET. *IEEE Nuclear Science Symposium*, 4:2035–2040, 2005.

[108] Siemens Medical Solutions Inc. LSO HI-REZ technology. Technical specifications. http://www.medical.siemens.com/siemens/zh_CN/gg_nm_FBAs/files/brochures/HI-REZ.pdf.

[109] Yuan-Chuan Tai et al. Performance evaluation of the microPET Focus: A third-generation microPET scanner dedicated to animal imaging. *J. Nucl. Med.*, 46(3):455–463, 2005.

[110] Y. Shao et al. Evaluation of hamamatsu R5900 series PMTs for readout of high-resolution scintillation arrays. *Nucl. Instrum. Methods Phys. Res. Sect. A*, 454(2):379–388, 2000.